Radii and neutron correlations of ^{6,8}He within the Gamow Shell Model

A Dissertation
Presented for the
Doctor of Philosophy
Degree
The University of Tennessee, Knoxville

Georgios Papadimitriou
December 2011

© by George Papadimitriou, 2011
All Rights Reserved.

Acknowledgements

The most important person regarding my Ph.D. was Witek Nazarewicz. It has been a privilege for me to work under his supervision. He was always there for me, to answer the many scientific questions I had, to teach me how to diagonalize complex matrices, to give me ideas for future scientific directions. This interest to me was shown in a daily basis, despite the fact he had countless other duties. The benefits for me were not only scientific but broader and important for a successful career in academia and also in life! He was a real mentor to me. Thank you very much, Witek.

At this point I should not forget my other collaborators: Nicolas Michel, Marek Płoszajczak, Jimmy Rotureau, and Andras Kruppa. Without them, the completion of this thesis would be a very difficult task. Nicolas Michel and Jimmy Rotureau especially gave me a lot of support in creating numerical routines and codes in C++, which was a completely unknown language for me when I started my journey in the nuclear many-body problem. The interactions I had with the other members of our group in ORNL and UT have also influenced me. I would like to thank Thomas Papenbrock, Gaute Hagen, Markus Kortelainen and Rolo Betan for the many interesting discussions we had all these years (in the case of Gaute it was not only physics!). I wish to thank from my heart the late Mario Stoitsov. Mario was a great physicist and a fantastic person. I really miss his company, his advices and his companion. The balance in a personal level was also very important to finish my thesis. I wish to thank my other half in life, Kim. Her patience and support during my Ph.D. years were extraordinary!

Abstract

We study the spatial correlations between halo neutrons in ^{6,8}He within the complex-energy Gamow Shell Model (GSM). To this end, we calculate the neutron and proton radii, and two-neutron correlations in a large shell model space consisting of the $0p_{3/2}$ resonance and non-resonant *psd* scattering continuum. We use schematic forces and the finite-range Modified Minnesota interaction. The calculated charge radii, corrected for the core polarization and spin-orbit effects, are compared to the values extracted from measured atomic isotope shifts. We find that the charge radius of ^{6}He primarily depends on the two-neutron separation energy and the shell-model occupation of the $0p_{3/2}$ orbit. We confirm that the ground-state GSM wave function of ^{6}He is dominated by the S=0 component representing a di-neutron structure. On the other hand, the correlation density of the 2^+_1 resonance in ^{6}He indicates a very weak di-neutron correlations in this state. We study the effect of pairing correlations on the neutron and charge radii of ^{6}He and we confirm the presence of the Pairing-Anti-Halo effect in this light system. Finally, we calculate the charge radius of ^{8}He in the full GSM space with the help of the Density Matrix Renormalization Group (DMRG) technique. The results of our realistic GSM+DMRG studies presented in this work show promise for extending the reach of the realistic complex-energy shell model to heavier halo systems.

Contents

List of Tables vii

List of Figures ix

1 Motivation and General Introduction 1

1.1 Nuclear physics outlook 1

1.2 Theoretical Methods 3

1.3 Coupling to the continuum manifestations 7

2 Theory and Experiment 11

2.1 Theoretical Framework 11

2.1.1 Single particle basis, model space, forces and parametrizations. 15

2.2 Experimental Charge radii 21

2.2.1 Factors that impact the charge radii of ^{6,8}He 23

3 Neutron correlations in ^{6,8}He nuclei 26

3.1 Neutron Correlations in ^{6}He nucleus 26

3.2 Neutron Correlations in ^{8}He nucleus 36

4 GSM calculations for ^{6,8}He nuclei 38

4.1 Radii operators and computation of radial integrals 38

4.2 Calculations with schematic forces 40

4.3 Calculations with the Modified Minnesota Interaction 43

4.3.1 ^{6}He nucleus 43
4.4 Pairing "anti-halo" effect in ^{6}He. 46
4.4.1 ^{8}He nucleus 50
4.4.2 GSM+DMRG application to the proton radius of ^{8}He 52
4.5 Concusions and Future Plans 61

Bibliography **64**

A Two body density and correlation density **75**
A.1 Matrix Elements of the correlation density 76

B Benchmark calculations between GSM and Complex Scaling **80**

Vita **83**

List of Tables

2.1 Convergence of the 0^+ g.s. energy of ^{6}He as a function of the HO radial nodes. The length of the oscillator parameter is b=2fm. The energies are in MeV. 15

2.2 Rms charge radii of ^{6,8}He, ^{11}Li, and ^{11}Be measured in recent experiments. 22

3.1 GSM Hamiltonian eigenvalues for the g.s of ^{6}He and some excited states. The values are in MeV. Experimental data are taken from [1]. Energies are expressed in the form E = E_r - i$\frac{\Gamma}{2}$, where Γ is the width. 26

3.2 Impact of the model space on the rms charge radius of ^{6}He 32

4.1 Point-proton radius of ^{6}He for different values of the surface parameter R_0 of SDI and SGI. All values are in fm. 42

4.2 Decomposition of the ^{6}He g.s wavefunction with schematic forces. . . 42

4.3 Decomposition of the ^{6}He wavefunction obtained with the MMN force. 44

4.4 Impact of the HO states used to represent the d-waves on the g.s energy and point-proton radius of ^{6}He. 50

4.5 Impact of the model space truncation on the energy and charge radius. 57

4.6 Energy and charge radius of ^{8}He for different truncation errors of the density matrix. The last column presents the maximum dimension of matrix to be diagonalized each time. See also Fig.(4.8) inset. 58

4.7 Comparison of the GSM rms charge radius with other theories and experiment. The values of the s.o contribution are also presented. Experimental values for the neutron and matter rms radii are taken from [2, 3, 4, 5, 6, 7, 8, 9]. 59

List of Figures

1.1 Theoretical methods used to solve the low energy nuclear many-body. The black area represents the valley of beta stability, while the yellow consists of the man-made radioactive nuclei. The green area consists of nuclei that are not made yet in laboratories, but they are expected to exist. On the right/left side the neutron/proton drip lines are denoted. The Figure is a courtesy of W.Nazarewicz from the SciDAC 2007 review (http://www.scidacreview.org/0704/html/unedf.html). 4

1.2 GSM calculations of the chemical potential and pairing field for ^{6,7,8}He. The chemical potential λ and the pairing Δ were extracted by using the approximate relations: $S_{2n}(N,Z) \approx -2\lambda$ and $S_{1n} \approx -\lambda-\Delta$ (for odd-N), $S_{1n} \approx -\lambda+\Delta$ (for even-N). 9

2.1 The Berggren ensemble in the complex k-plane. The resonant and scattering states lying along the L_+ contour in the fourth quadrant are indicated. 12

2.2 The COSM coordinate system used in our GSM calculations: (a) the ^{6}He case; (b) the general case of a system containing a core and n-valence particles. 14

2.3 Possible geometries of halo neutrons with respect to the α core in ^{6}He (a) and ^{8}He (b and c). 25

3.1 Contour plots of the two body correlation density in ^{6}He. In the upper panel is shown the total correlation, while the middle and bottom show the S=0 and S=1 components respectively. Notice the radial tail of the S = 0 component. 27

3.2 Contour plots of the two body correlation density in ^{6}He. In the top panel is shown the correlation density when the two-body interaction is switched off, while in the bottom panel we use a MMN interaction in a restricted p-shell model space 30

3.3 Angular densities of the ^{6}He g.s. 32

3.4 Correlation density of the 2^+ state of ^{6}He. The left top panel shows the total density, while the left and right bottom the S=0 and 1 channels respectively. In the right top panel we present the correlation density when the two-body interaction is turned off. The calculation is performed in a p-sd model space. 33

3.5 Angular densities of the ^{6}He 2^+ excited state. 35

3.6 Correlation densities of the ^{8}He 0^+ excited state. 36

3.7 Angular 2n GSM densities (S=0, 1, and total) for g.s. configurations of ^{6}He (solid lines) and ^{8}He (dashed lines). 37

4.1 Radial halo density of ^{6}He calculated in GSM with **SGI** interaction. Since ^{6}He is a bound system, its valence neutrons are localized in space. Consequently, the integral (4.4a) involving the r^2 operator can be cut around 20 fm. The inset shows the radial density together with the radial form factor of the s.p. WS potential used to generate the Berggren basis. The number of contour discretization points N_{sh} is indicated. 39

4.2 Evolution of the rms charge radius of ^{6}He as a function of the two-neutron separation energy for the MMN force. The two different curves correspond to i) changing the MMN strength (black) and ii) changing the WS strength (red). See text for details. The experimental values are included for comparison. 43
4.3 Comparison between the realistic AV18 force and the MMN used in this work. With π is denoted the one-pion exchange region. 45
4.4 Similar to Fig.4.2 but for the rms neutron radius of ^{6}He. For the neutron rms the data were taken from [4]. 47
4.5 Dependence of the interaction energy, calculated as the expectation value of the two-body interaction (top panel) and correlation angle (bottom panel) of ^{6}He as a function of the two-neutron separation energy for the MMN force. The two different curves correspond to i) changing the MMN strength (black) and ii) changing the WS strength (red). See text for details. 48
4.6 Angular densities of the ^{6}He g.s. It is shown the density when the $S_{2n} = 0$ MeV for the case of a very broad (shallow WS potential) $p_{3/2}$ resonance (red curve) and when $S_{2n} = 0$ MeV but for a weak two-body interaction. 49
4.7 Radial density of the halo neutrons in ^{6}He in a full calculation (red) as compared to the calculation where the d-waves were represented by HO states. 51
4.8 Convergence pattern of the real part of the energy in ^{8}He as a function of the ϵ. In the inset shows the dimension of the DMRG matrix versus ϵ. 55
4.9 Convergence pattern of the charge radius in ^{8}He as a function of the ϵ. 56

4.10 Different contributions to the charge radius of ^{6}He (solid line, squares) and ^{8}He (dashed line, dots) calculated in GSM. The core swelling contribution is taken from GFMC calculations of Ref. [10]. Recently revised experimental charge radii come from [11] (triangles). The NCSM [12] (stars) and GFMC [13] (pentagons) results are marked for comparison. The inset shows GSM rms neutron radii compared to experiment [8]. 60

A.1 Comparison of the correlation densities in three different coupling schemes. 78

B.1 Energies and root mean square radii between GSM and Complex Scaling (CS). 80

B.2 Comparison of correlation densities between GSM and Complex Scaling (CS). 82

Chapter 1

Motivation and General Introduction

1.1 Nuclear physics outlook

Nuclear physics is the study of structure of nuclei and the interactions between the nucleons. The main goal of nuclear structure is to develop a comprehensive description of all nuclei and their reactions [14]. This task can be achieved by answering overarching questions such as:

- What is the nature of the force that binds nuclei and how this force is modified in exotic regions of the nuclear chart?
- What is the impact of the nuclear medium on properties and spectra of exotic nuclei?
- Do we have a clear understanding of the reactions that take place in the Sun and are important for our existence?

The benefits from answering these questions will not be only scientific, but they can also have an impact on our society because of the energy problems we are facing. For example a question that arises is:

- How can we use our knowledge of nuclear structure to construct nuclear reactors without proliferation problems and with limited burning material?

Attempting answering these questions lead to a renewed interest of physics of nuclei and we are witnessing a tremendous progress in both theory and experiment. From the theoretical point of view, studies of exotic nuclei resulted in the birth of a new field in nuclear physics which is constantly growing; this is the study of Open Quantum Systems (OQS) i.e., systems that interact with the external environment [15, 16]. The physics of OQSs has attracted a lot of attention in many other fields of physics (atomic and molecular physics, condensed matter physics and quantum optics). It is indeed possible to control experimentally the coupling of the system to the continuum allowing scientists to study the different behavior of the system in different regimes of "openness". Examples are the laser induced continuum structures in atoms [17], open micro-wave cavities [18] and the tuning of Feshbach resonances by an external magnetic field [19]. In atomic nuclei the "openness" of the system is expressed through the radiative captures and decays away from the valley of stability. In this sense atomic nuclei must be seen as a network of strongly correlated fermionic systems interconnected via reaction and decay channels. Many properties of these different exotic systems are generic and common to all weakly bound or unbound systems close to the continuum [20, 21, 22]. The study of OQS provide an interdisciplinary field of research where ideas and methods from many different areas of physics mathematics and computer science overlap. The complex nature of the resonances and the continuum states requires us to deal with non-Hermitian operators and requires a formulation of quantum mechanics in a rigged Hilbert space (Gelfand triplet) [23, 24, 25]. Additionally the inclusion of many continuum degrees of freedom makes their description computationally demanding, calling for the development of sophisticated algorithms and theories which will enable scientists to use high performance super computing facilities [26, 27, 28, 29].

On the experimental side recent advances in rare isotope facilities around the world, open a new window of exploration of nuclei far way of the stability. One of the recent achievements of this attempt was the determination of the charge distribution of neutron-rich Helium isotopes (^{6,8}He) with a measured accuracy reaching the 1%. Charge radii of helium halo represent a splendid example of the cross-fertilization between atomic and nuclear physics for the description of OQSs. They were extracted from measured isotopic shifts of helium atoms [30, 31, 11] using high precision atomic theory calculations and simultaneously, because of their precision they provide a critical test for the nuclear Hamiltonian itself. Since the charge in helium halos is contained in the tightly bound α-core, the differences in the charge distributions reflect the interactions and correlations amongst the valence neutrons.

1.2 Theoretical Methods

One of the basic themes in low energy nuclear structure calculations is the determination of the force acting between the nucleons. Contrary to other fermionic problems, dealing with atoms and molecules, there is no derivation up to now of the nucleon-nucleon force from first principles, i.e. from Quantum Chromodynamics (QCD). The key point in low energy nuclear structure is the identification of the relevant degrees of freedom. Even though QCD is the underlying theory that should serve as a starting point, in the MeV region the relevant degrees of freedom are the colorless nucleons. This realization was applied recently in the construction of the nucleon-nucleon Hamiltonian, based on methods which stem from the Effective Field Theory (EFT) [32, 33, 34, 35, 36]. Having obtained the nuclear Hamiltonian the methods that are used to compute nuclear observables are the same as in any other many-body problem (atoms, molecules etc). These are the ab-initio methods, the Configuration Interaction (CI) shell model and the Density Functional Theory (DFT) (Fig.1.1).

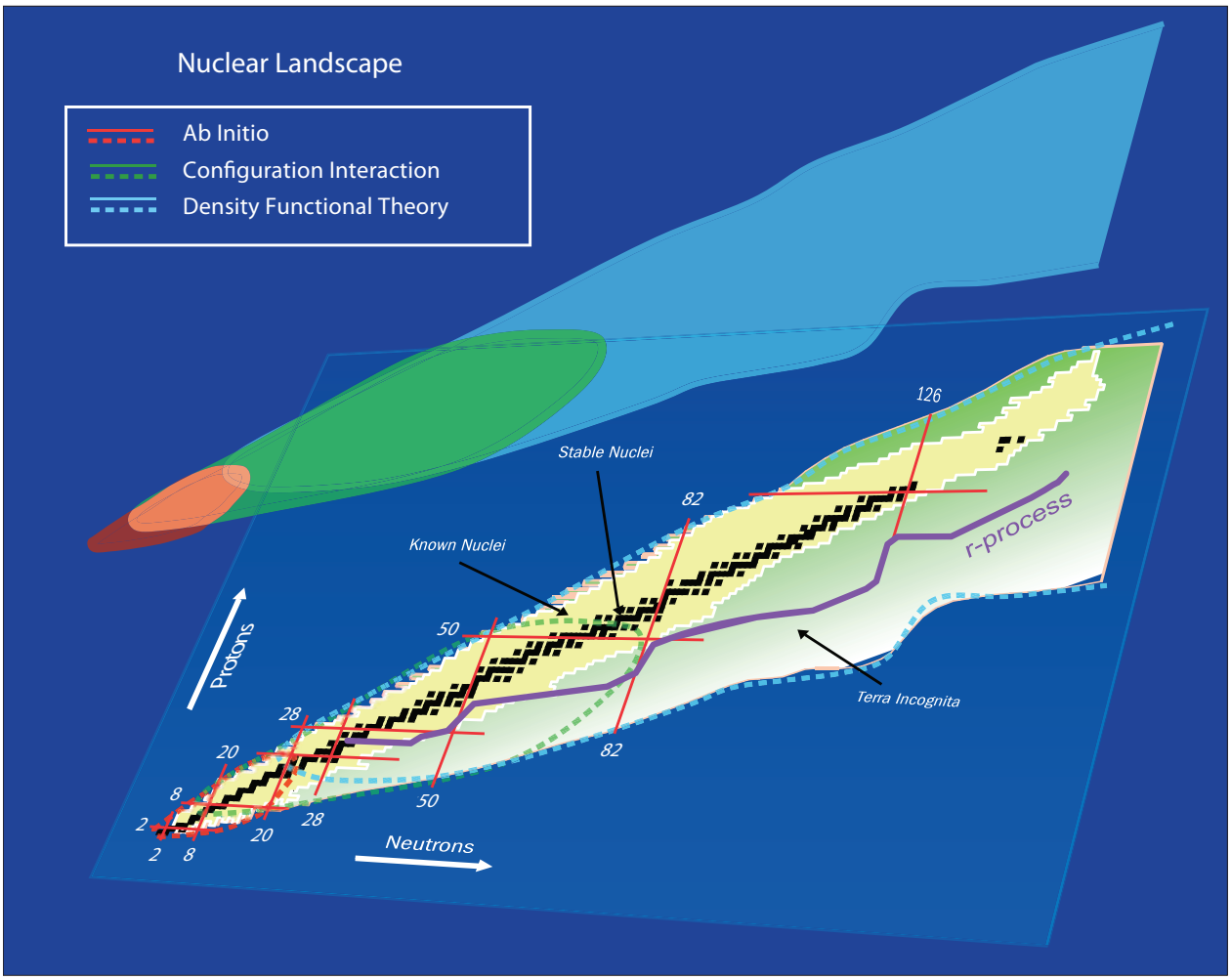


Figure 1.1: Theoretical methods used to solve the low energy nuclear many-body. The black area represents the valley of beta stability, while the yellow consists of the man-made radioactive nuclei. The green area consists of nuclei that are not made yet in laboratories, but they are expected to exist. On the right/left side the neutron/proton drip lines are denoted. The Figure is a courtesy of W.Nazarewicz from the SciDAC 2007 review (http://www.scidacreview.org/0704/html/unedf.html).

Ab-initio methods: The basic concept is that one solves the nuclear many body problem where all the particles are active, i.e the full A-particle problem, with A being the sum of protons and neutrons. The commonly used methods are the No Core Shell Model (NCSM) [37], the Green's Function Monte Carlo (GFMC) [13, 38] and the Coupled Cluster Theory (CCT) [39]. The interactions that are used are the so called realistic interactions, which are fitted to reproduce nucleon-nucleon

elastic scattering phase shifts and selected few body observables. These realistic forces can be of a phenomenological type, such as the Argonne v18 and the CD-Bonn 2000 [40, 41], or constructed by an effective Lagrangian consistent with the QCD symmetries [35, 36]. The ab-initio techniques have certain limitations, since dimensionality problems arise by increasing the number of particles. Additionally the realistic potentials have the characteristic of the very strong short-range repulsion ("hard-core") which causes the particles to scatter in very high energies, making unavoidable to use very large model spaces and hence a tremendous computational effort. With the help of renormalization techniques (we refer to the reader to [42] for a comprehensive review) the "hard-core" problem is treated successfully but still the methods are limited to the computation of light nuclei. Furthermore, it was soon realized that two-body forces alone, do not give very satisfactory results for the spectra and masses of these light species [13]. The neglect of quark degrees of freedom and the renormalization of the short-ranged repulsive part of the interaction, generates many body forces [42]. Coping with huge dimensions and implementing many-body forces in their framework constitute the basic challenges for the ab-initio methods.

CI methods: For the calculation of heavier nuclei a common many-body method is the CI or Shell Model (SM) [43] for a review. The basic theme is again the diagonalization of the Hamiltonian matrix in a suitable basis. The space of configurations is truncated in two steps: First, configurations that correspond to a system of protons and neutrons that form a system of closed shell orbits are assumed to represent a closed core. An example is ^{18}O where instead of solving the 18-body Schrödinger equation, is assumed that ^{16}O is a closed core, and the problem is reduced to a two-body problem. The second step is related to the space that the active (or valence) particles are allowed to move. This is the model space of the Shell Model calculation. The interactions that are used can be of microscopic nature where G-matrix techniques [44] are applied to renormalize the interaction in a given model space or phenomenological where the parameters of the force are

fitted to available experimental data (masses, radii, spectra etc). The dimensions of the problem grow really fast with the increase of valence particles and powerful computational techniques such as the Shell Model Monte Carlo (SMMC) [45, 46] and the Density Matrix Renormalization Group (DMRG) [47, 48, 49, 29, 50] are employed to cure the dimensionality catastrophe.

Density Functional Theory: For heavier systems the tool of choice is the Density Functional Theory [51]. It is based on the ansatz that the ground state energy of the system is a unique functional of the nucleonic density. In this way the computational cost scales in a smoother manner as compared to the previous methods. This theory can be applied to a wide range of nuclei along the nuclear chart and the big challenge is to construct the universal energy density functional [52, 53].

These are the basic theories that are applied to compute nuclear properties along the nuclear chart. But most of the states of a nucleus are embedded in the continuum of decay channels due to which they get a finite lifetime, i.e. discrete states change into resonances with a complex energies E_i-$i\frac{\Gamma_i}{2}$, where E_i is the centroid energy of the state, while Γ_i is the width related to the lifetime of the state. In order to be able to describe resonances and scattering states in the same framework, modifications of the existing theories should take place. Extensions of the ab-initio methods to include continuum degrees of freedom have been successfully applied to describe structure and reaction properties of light nuclei. Examples are the NCSM combined with the Resonating Group Method (RGM) [27], the GFMC generalized for the description [26] of reactions, and the CCT where the Harmonic Oscillator (HO) basis was substituted by the Berggren ensemble which contains resonant and non-resonant scattering states [54]. We also find the Continuum Shell Model (CSM) [55] and the parented Shell Model Embedded in the Continuum (SMEC) [56]. These are CI methods in the real energy plane, where the coupling to the external environment is taken into account by applying Feshbach projection techniques. Recently the multiconfigurational Shell Model in the complex energy was introduced, the so called Gamow Shell Model (GSM) [57] and more details for this approach will be given in forthcoming chapters. The

Complex Scaling (CS) [58] method is another successful method, which is based on the complex rotation of a Hermitian Hamiltonian in the complex energy plane. For medium mass and heavy nuclei DFT methods are also suitable to treat the coupling to the continuum. When the DFT equations are solved in the coordinate representation, the continuum is taken into account by box discretization techniques [59, 60], while if one chooses the solution by means of basis expansion, proper asymptotic behavior should be imposed on the radial wavefunctions. The latter method is know as Gamow Hartree Fock Bogoliubov (GHFB) [61] and shares many similarities with the GSM in the description of resonances.

1.3 Coupling to the continuum manifestations

The proximity of the continuum can alter in a dramatic way the properties of the nucleus [20]. One example is the appearance of halo states very close to the particle emission thresholds. Halo nuclei are characterized by an extremely dilute neutron matter as a consequence of the very weak binding and the tunneling of the radially extended wavefunctions into classically forbidden regions. In this region the pairing correlations are strongly modified by the continuum and they can be responsible for the existence or not of a particular nucleus. A manifestation of this phenomenon is the appearance of Borromean halo nuclei, which are defined as the systems which the A and A-2 systems are bound, but the A-1 is unbound. Another phenomenon is the extreme clusterization observed in halo systems. The valence particles are spatially decoupled from a relatively bound core, forming a strongly correlated state.

The continuum coupling has also a pronounced effect on the spectra of nuclei. One example is the striking asymmetry of the spectra of some mirror systems. This phenomenon is known as the Thomas-Ehrman shift [62, 63] and owes its explanation in the generic features of the coupling to the continuum. Since the isospin is a symmetry that is well preserved in nuclear physics (to a large extent at least), this large asymmetry of some mirror nuclei spectra is closely related to the different

proton/neutron emission thresholds and the proximity of the continuum. The isospin breaking effect due the coupling to the continuum, has been studied recently within the GSM [64]. The degree of the symmetry breaking strongly depends on the angular momentum of the state, and it is more enhanced for low ℓ states. This specific angular momentum dependence has also been observed on scattering cross sections and Spectroscopic Factors (SFs). The phenomenon is known as the Wigner-cusp effect and it is explained by the Wigner threshold law [65]. It was found experimentally that the cross section is characterized by a cusp for energies close a reaction threshold. This phenomenon is universal and can be found in other branches of physics (electron-atom scattering, ultracold atoms scattering etc). It is characterized by a specific behavior of the cross-section or the SF in the vicinity of the emission threshold. In particular the behavior is ($-S_{1n}^{\ell-1/2}$) below and ($S_{1n}^{\ell+1/2}$) above the threshold. It was shown, in the framework of the GSM [66, 67], that this behavior can be observed only when the scattering continuum (environment coupling) is accounted for. These phenomena are universal and do not depend on the fine details of the underlying Hamiltonian, but only on the positions of the emission thresholds. It is very important hence to employ a theory that treats continuum degrees of freedom rigorously and for this reason GSM is a tool of choice.

To this end we use a criterion for when the coupling to the continuum can be of particular importance. Using a formula [60, 68] that relates the separation energy with the chemical potential λ_n and the pairing field Δ_n ($S_n \approx \lambda_n - \Delta_n$) we observe that for small values of separation energy the chemical potential and the pairing are of the same order of magnitude. The direct implication of this realization is that the many-body correlations, which are represented by the pairing field, are of the same importance as the single particle field governed by the chemical potential. Hence the very notion of the single particle motion in a mean field potential is under question in weakly bound nuclei (the strong many-body correlations change this picture). As we see in Fig.(1.2), this is the case for ^{6,8}He and hence, it is expected that the continuum will have an important impact on their properties.

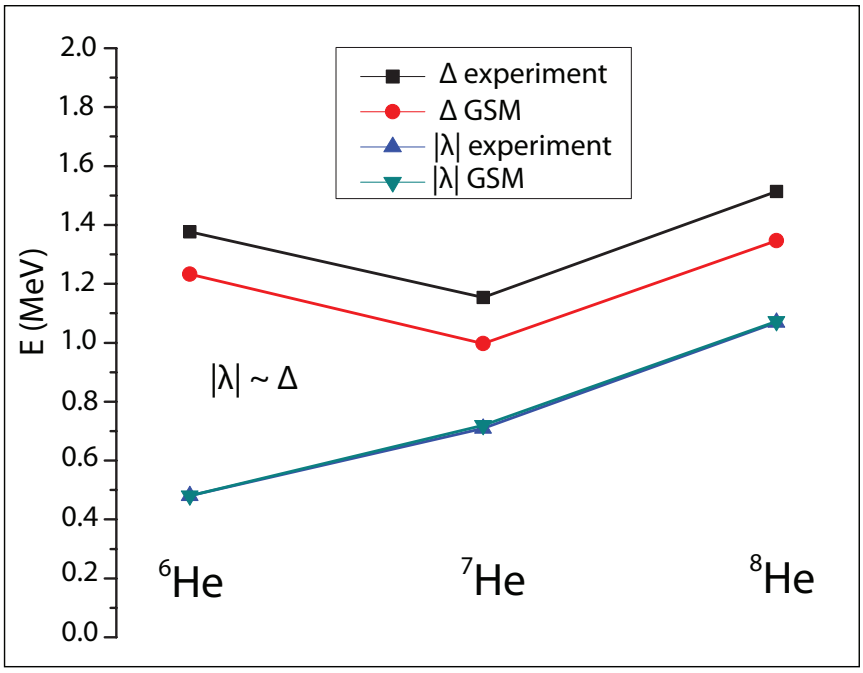


Figure 1.2: GSM calculations of the chemical potential and pairing field for ^{6,7,8}He. The chemical potential λ and the pairing Δ were extracted by using the approximate relations: $S_{2n}(N,Z) \approx -2\lambda$ and $S_{1n} \approx -\lambda-\Delta$ (for odd-N), $S_{1n} \approx -\lambda+\Delta$ (for even-N).

The following chapters constitute a lightly revised version of two papers and one proceeding article. One of them with title: *Charge radii and neutron correlations in helium halo nuclei* has been submitted on Physical Review C as a Rapid Communication in 2011 by George Papadimitriou, Andras Kruppa, Nicolas Michel, Witek Nazarewicz, Marek Płoszajczak and Jimmy Rotureau. The second one with title: *Halo neutrons in ^{6,8}He in the Gamow Shell Model* is in preparation by the same authors. The proceeding article was published on (AIP Conf. Proc. 1128, 11 (2009)), as a contribution from the 5th ANL/MSU/JINA/INT FRIB Workshop on Bulk Nuclear Properties that took place in Michigan State University on November 19-22, 2008. My use of "we" in the following, refers to my co-authors and myself. My primary contributions to the papers include: (1) most of the calculations, which included derivation of formulas (radii and neutron correlations). Also the calculation of new observables, such as radii, correlations and spin-orbit correction, required

numerical coding. I also contributed in a benchmarking work between GSM and CS. (2) major part of the writing and editing.

Chapter 2

Theory and Experiment

2.1 Theoretical Framework

The primary idea behind the GSM is to replace the Harmonic Oscillator (HO) basis, which is suitable for the description of systems close the valley of stability, by the Berggren ensemble [69]. The Berggren basis is generated by a finite-depth, single-particle (s.p) potential, which can be taken as an average Woods-Saxon (WS) potential or more microscopic Hartree-Fock (HF) potential obtained from the two-body effective interaction. The resonant states are the eigenstates of the generalized s.p Schrödinger equation corresponding to the outgoing boundary conditions; they represent the poles of the one-body S-matrix. As shown in the pioneering work by Berggren [69], the resonant (bound and decaying) states $|u_n\rangle$, together with the complex-energy scattering states along the contour L_+ in the fourth quadrant of the complex k-plane, form a complete set:

$$\sum_n |u_n\rangle\langle\tilde{u_n}| + \int_{L_+} |u_k\rangle\langle\tilde{u_k}|\, dk \;\; = 1. \tag{2.1}$$

This ensemble enables us to expand any function with outgoing asymptotics $\exp(ikr)$, where k lies between the contour L_+ and the real k-axis. There exist a number of completeness relations which include more general contours and also resonant states

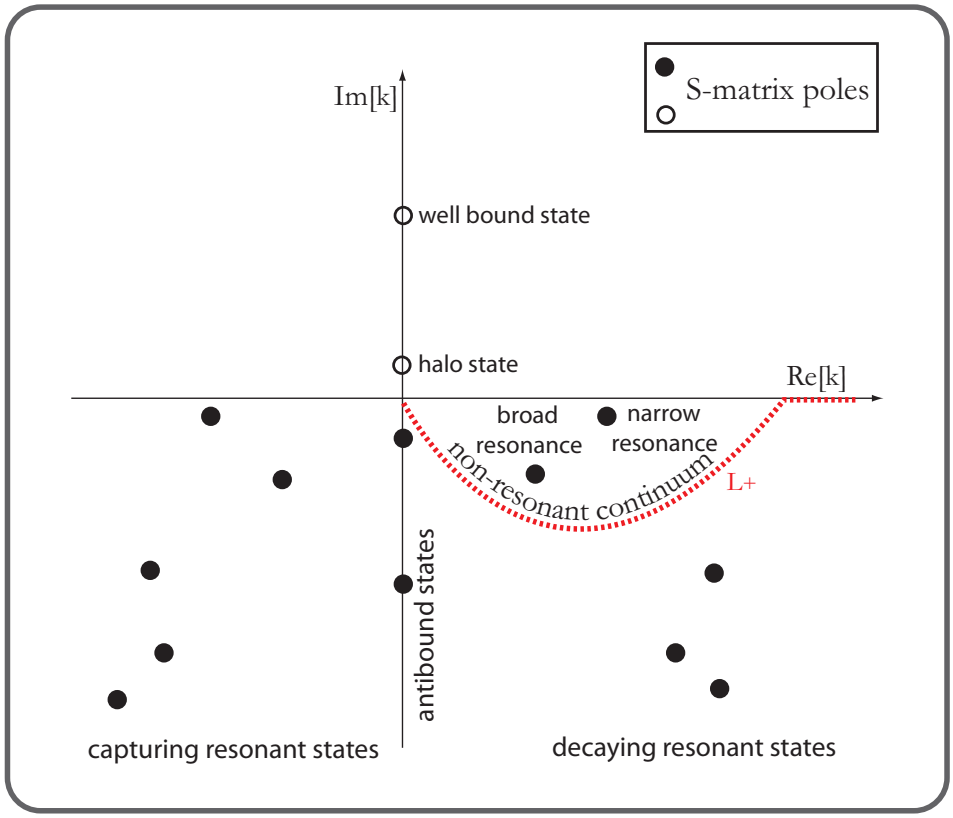


Figure 2.1: The Berggren ensemble in the complex k-plane. The resonant and scattering states lying along the L_+ contour in the fourth quadrant are indicated.

that lie in different quadrants of the k-plane [70]. We use the specific representation (2.1) because we are interested in the particle decay of the system. In practical applications, the contour integral over the scattering states is discretized by means of the Gauss-Legendre quadrature rule, and we end up with a discrete completeness relation:

$$\sum_n |u_n\rangle\langle\tilde{u_n}| + \sum_{i=1}^{N} |u_i\rangle\langle\tilde{u_i}| \simeq 1. \tag{2.2}$$

From this discretized s.p basis which manifestly contains bound, resonant, and non-resonant continuum states, we construct a many body basis of Slater determinants. Due to the appearance of complex-energy basis states, the Hamiltonian matrix is no longer Hermitian, but complex-symmetric. The matrix elements are properly regularized by means of the exterior complex scaling method [71]. For earlier

applications of the GSM model to light nuclei and threshold phenomena, we refer the reader to Refs. [57, 72, 73, 74]

The GSM results should be free from spurious center-of-mass (CM) motion. This spuriousity stems from the fact that the many-body wave function depends on $3A$ nucleonic coordinates whereas the intrinsic properties of a nucleus depend only on $3A-3$ independent coordinates. In the standard Shell Model approach, the Lawson [75] method is often applied to separate the internal and CM motion. Other approaches used to factorize out the CM motion make use of the Jacobi coordinates and the Hyperspherical Harmonics expansion method [76]; those are computationally intensive procedures due to antisymmetrization effects, especially when the number of particles is increased. In our GSM approach, we adopt a system of coordinates inspired by the Cluster Orbital Shell Model (COSM) [77] illustrated in Fig.(2.2). These coordinates are purely intrinsic since they are taken with respect to the core; hence, the resulting GSM Hamiltonian is free from CM spuriosity. Antisymmetrization effects do not introduce any additional computational difficulty. In the COSM coordinates, the GSM Hamiltonian takes the form:

$$H=\sum_{i=1}^{n}\left[\frac{p_i^2}{2\mu}+U_i\right]+\sum_{i<j}^{n}\left[V_{ij}+\frac{1}{A_c}\mathbf{p}_i\mathbf{p}_j\right], \tag{2.3}$$

where μ is the reduced mass of the valence particles, V_{ij} is the two-body interaction, and $\mathbf{p}_i\mathbf{p}_j$ is the two-body energy recoil term with A_c being the mass of the core.

The appearance of the recoil term in (2.3) is the only practical difference compared to the previous GSM applications, except for the recent paper on mirror symmetry breaking [64].

Matrix elements of the recoil term for scattering states can sometimes diverge and need to be regularized. We treat the recoil matrix elements by using the Harmonic Oscillator (HO) expansion method described in [78] and also applied recently in GSM calculations for the study of isospin breaking in weakly bound systems [64]. In this approach, formulated in the coordinate representation, the momentum operator $\mathbf{p}_i$ is

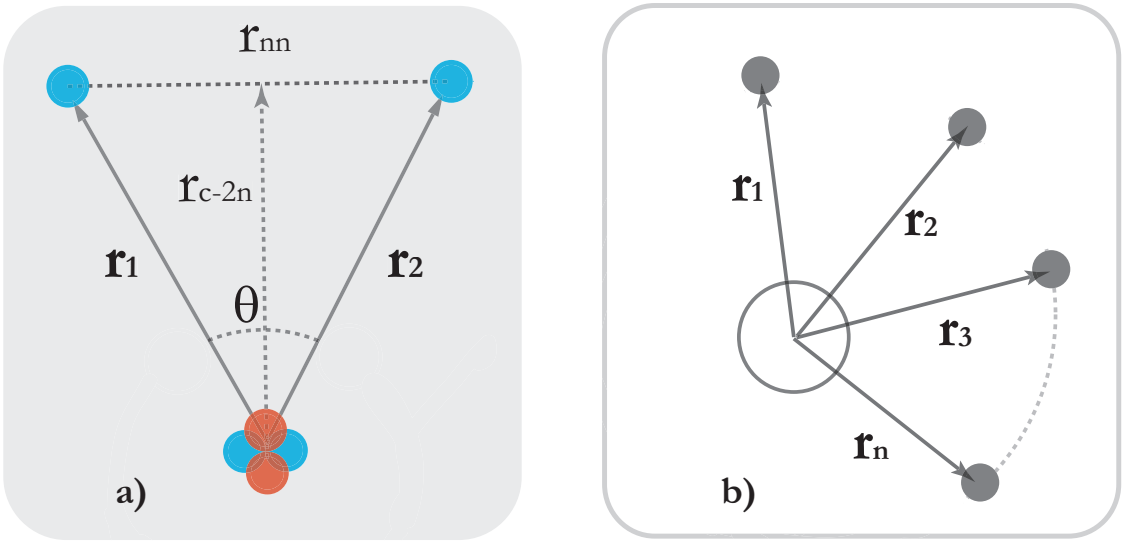


Figure 2.2: The COSM coordinate system used in our GSM calculations: (a) the ^{6}He case; (b) the general case of a system containing a core and n-valence particles.

expanded in an HO oscillator basis

$$\mathbf{p}_i = \sum_{\alpha\gamma} |\alpha\rangle\langle\alpha|\mathbf{p}_i|\gamma\rangle\langle\gamma|. \tag{2.4}$$

The matrix elements of $\mathbf{p}_i$ between the Gamow states $|a\rangle$ and $|c\rangle$ are given by

$$\langle a|\mathbf{p}_i|c\rangle = \sum_{\alpha\gamma} \langle a|\alpha\rangle\langle\alpha|\mathbf{p}_i|\gamma\rangle\langle\gamma|c\rangle. \tag{2.5}$$

Here we notice that the numerical effort involves calculations of the overlaps $\langle a|\alpha\rangle$ and $\langle\gamma|c\rangle$ between Gamow states and HO states. Because of the Gaussian asymptotic behavior of the HO wave functions, no complex scaling is needed, since these overlaps always converge. In the present work we adopted the HO expansion for the recoil. The length parameter of the HO was chosen to be $b = 2$fm. We used a total of $n_{max} = 16$, were n_{max} is the radial quantum number ($N = 2n + l$). This number was established through benchmarking with the CS calculations [79]. For this number

the manybody solution has no dependence on the parameter b. We should mention

Table 2.1: Convergence of the 0^+ g.s. energy of ^{6}He as a function of the HO radial nodes. The length of the oscillator parameter is b=2fm. The energies are in MeV.

n_{max}	$J^\pi=0^+$
4	-0.945
6	-0.965
8	-0.974
10	-0.9745
12	-0.975
14	-0.975
16	-0.975
18	-0.975

that the matrix elements (2.5) exhibit a slow convergence by increasing the number of HO quanta due to the long-range character of $\mathbf{p}_i$. However, this behavior does not cause any practical difficulty as the eigenvalues and eigenfunctions of the GSM eigenproblem do converge, see Table 2.1.

2.1.1 Single particle basis, model space, forces and parametrizations.

Single particle basis and model space

In the following, our single particle basis was generated by a Woods-Saxon potential which consists of a central and a spin-orbit term:

$$V(r) = -V_{WS} \cdot f(r) - 4.0 V_{so} (\mathbf{l} \cdot \mathbf{s}) \frac{1}{r} \left| \frac{df(r)}{dr} \right| \tag{2.6}$$

with V_{WS} , V_{so} being the strength parameters and

$$f(r) = \left[1 + \exp\left(\frac{r - R_0}{d} \right) \right]^{-1} \tag{2.7}$$

is the WS form factor characterized by radius R_0 and diffuseness d. These parameters are fitted to reproduce the energy and width of the $\frac{3}{2}^-$ and $\frac{1}{2}^-$ ($0p_{3/2}$ and $0p_{1/2}$ in our model) states of ^{5}He [72, 73]. For systems with A>6 the quality of the aforementioned basis deteriorates, leading in some cases in poor convergence with respect to the basis size. The remedy for this behavior is to use a s.p basis that is optimal for a given nucleus, that is the GHF basis. The starting point for the creation of the GHF potential is of course the initial WS fitted to ^{5}He. A detailed and technical description of the GHF method could be found in [80].

The large valence space contains five partial waves ($p_{3/2}$,$p_{1/2}$,$s_{1/2}$,$d_{5/2}$ and $d_{3/2}$) with the $0p_{3/2}$ resonant state also included in the calculation. The $p_{3/2}$ contour is taken to be complex as a consequence of the Berggren completeness relation (2.1). The role of the non-resonant $p_{3/2}$ states is to cancel the imaginary part of the resonant state that is included in the basis. For the same reason all the remaining partial waves can be taken along the real axis, since the corresponding resonant states are not included. Inclusion of the very broad $0p_{1/2}$ resonant state would result in taking the $p_{1/2}$ continuum as complex. This leads to considering many $p_{1/2}$ non-resonant shells (discretization points) so as to satisfy the completeness, however we have noticed that this inclusion has a very small impact on the renormalization of the force. Hence, there is no conceptual gain in the inclusion of the $0p_{1/2}$ resonant state, at least for the Helium isotopes. The valence neutrons in ^{6,8}He cannot occupy the 0s orbit which is already occupied by the core neutrons. To take this into account we employ the Saito's Orthogonality Condition Model (OCM) [81]. The s.p Hamiltonian h is substituted by the

$$\tilde{h} \rightarrow php$$

where $p = 1 - |0s_{1/2}\rangle\langle 0s_{1/2}|$ and the $0s_{1/2}$ is assumed to be given by a HO state of b=1.4fm that reproduces the observed charge radius of ^{4}He. This method guarantees that all the i$s_{1/2}$ states be orthogonal to the $0s_{1/2}$ wavefunction of the core and the Pauli principle is satisfied.

Forces.

In our calculations we used as residual two-body interactions the Surface Delta Interaction (SDI) [82], the Surface Gaussian Interaction (SGI) [74] and a finite range interaction which resembles the Minnesota force [83]. The basic difference amongst these forces lies on their range, i.e., SDI has a zero-range, MN has a finite-range and the SGI is a compromise between a zero-range and a finite range force. Their analytical form is given below:

$$V^{\rm SDI}(1,2) = -V_0^{\rm SDI}\delta(\mathbf{r}_1-\mathbf{r}_2)\delta(|\mathbf{r}_1|-R_0) \tag{2.8}$$

$$V^{\rm SGI}_{J,T}(1,2) = -V_0(J,T)\exp\left[-\left(\frac{\mathbf{r}_1-\mathbf{r}_2}{\mu}\right)^2\right]\delta(|\mathbf{r}_1|+|\mathbf{r}_2|-2R_0) \tag{2.9}$$

$$V^{\rm MN}(1,2) = \left(V_R+\frac{1}{2}(1+P^\sigma_{ij})V_t+\frac{1}{2}(1-P^\sigma_{ij})V_s\right)\left(\frac{1}{2}u+\frac{1}{2}(2-u)P^\tau_{ij}\right) \tag{2.10}$$

In the following we provide some details on the interactions. Historically the SDI was the first interaction used in GSM calculations [72]. It has a zero-range and also peaks on the nuclear surface through the R_0 parameter (2.8). The reason for choosing this interaction is twofold. Firstly, it incorporates the fact that the residual nuclear interaction takes place mostly on the nuclear surface due to the Pauli principle. Secondly, the two-body matrix elements can be easily calculated and no complex scaling is needed. It is not the purpose of this article to mention all the technical details of computing integrals in the GSM, however it is worth mentioning, that integrals between scattering states are difficult to calculate and they can lead to Dirac delta functions coupling different partial waves. The disadvantage of the SDI is that it generates a cut-off energy dependence due to its zero-range character.

The next interaction that we employed is the SGI (2.9). By inspecting SDI and SGI we see that the only practical difference lies in the replacement of one delta function with a Gaussian form factor, while the second delta function is kept for the same reasons as in the SDI. The appearance of a Gaussian form factor makes the GHF

potential well defined in coordinate space, enabling us to employ the GHF method for each nucleus under consideration [74].

The third interaction used is a fully finite range interaction. In (2.10) the form factors V_R, V_t and V_s are taken to have the following Gaussian forms:

$$\begin{aligned} V_R &= V_{0R} \exp(-\kappa_R r_{ij}^2), \\ V_t &= V_{0t} \exp(-\kappa_t r_{ij}^2), \\ V_s &= V_{0s} \exp(-\kappa_s r_{ij}^2) \end{aligned} \tag{2.11}$$

The MN potential strength parameters and the ranges of these Gaussian form factors were determined so as to reproduce the $n-p$ triplet and $p-p$ singlet s-wave effective range parameters [83]. One of them has a repulsive character, imitating the hard nuclear core and the other two are attractive, acting on the spin singlet and spin triplet channels. The MN parameters are:

$$\begin{aligned} V_{0R} &= +200\text{MeV}, \kappa_R = 1.487\text{fm}^{-2} \\ V_{0t} &= -178.0\text{MeV}, \kappa_t = 0.639\text{fm}^{-2} \\ V_{0s} &= -91.85\text{MeV}, \kappa_s = 0.465\text{fm}^{-2} \end{aligned} \tag{2.12}$$

One should again notice the short range Gaussian (κ_R=1.487fm^{-2}) has a repulsive strength mimicking the short range nuclear repulsion, while the "long" range parts are attractive. Usually a Gaussian MN central force is written as:

$$\begin{aligned} &V(1,2) = \\ &\sum_{k=1}^{3} V_{k0} \left(W_k - M_k P^\sigma P^\tau + B_k P^\sigma - H_k P^\tau\right) f(\mathbf{r}_{12}) \end{aligned} \tag{2.13}$$

where $f(\mathbf{r}_{12})$ is a Gaussian form factor with three different ranges. The interaction is given as a function of the relative internucleon distance $r_{12} = |\mathbf{r}_1 - \mathbf{r}_2|$. In the general case the parameters W_k, M_k, B_k and H_k are independent from each other and their values are to be determined by fitting them to data. However, in the MN case they are expressed in terms of one mixing parameter u:

$$\begin{aligned} W_1 = \frac{u}{2}, M_1 = \frac{2-u}{2}, B_1 = 0, H_1 = 0 \\ W_2 = \frac{u}{4}, M_2 = \frac{2-u}{4}, B_2 = \frac{u}{4}, H_2 = \frac{2-u}{4} \\ W_3 = \frac{u}{4}, M_3 = \frac{2-u}{4}, B_3 = -\frac{u}{4}, H_3 = -\frac{2-u}{4} \end{aligned} \tag{2.14}$$

This mixing parameter was determined to be $u = 0.970$ in the initial paper [83], but we shall use the value u=1. The reasoning behind this change is the following: for the Helium isotopes there is only one isospin channel active (T=1). For T=1 the isospin exchange operator $\mathrm{P}^\tau = 1$ and it is a matter of algebra to realize that only two Gaussians are necessary for the description of T=1 systems. These are the repulsive V_{0R} and the attractive spin singlet V_{0s}. We thus reduced the number of force parameters adjusted to experimental data to only two (the ranges are taken as in (2.12)). We have observed that even with u=0.970 the dependence of the results on V_{0t} is weak. As it was stated again [83], especially for light systems, the mixing parameter is close to unity. For heavier systems its value departs from unity and it should be included in the calculation, increasing the number of parameters of the central part by two (both u and V_{0t} should be determined). In the general case of a central force, the parameters to be determined are twelve, assuming that the ranges of the Gaussians are not considered in the fit. For our GSM applications we leave the ranges unchanged, since they incorporate all the short-range physics which we do not want to play with, but we modify the strengths in a manner that will be explained later. In order to avoid divergences when calculating integrals, we use the method of HO expansion already discussed in the context of the recoil term. Following this

procedure, the two-body matrix elements of the interaction read:

$$\langle a\, b|\hat{V}|c\, d\rangle = \sum_{\alpha\,\beta\,\gamma\,\delta}^{N_{max}} \langle \alpha\,\beta|\hat{V}|\gamma\,\delta\rangle\langle a|\alpha\rangle\langle b|\beta\rangle\langle c|\gamma\rangle\langle d|\delta\rangle \tag{2.15}$$

We used b=2fm and n_{max} =16 (N=2n+l) as in the case of the recoil operator expansion. In order to calculate matrix elements of the original interaction in a Gamow basis, where the single particle basis functions depend on $\mathbf{r}_1$ and $\mathbf{r}_2$, would require to perform a multiple expansion or Slater decomposition. However, if the matrix elements are calculated between HO states (2.15), this expansion is not necessary. The interaction is kept intact and the so called Brody-Moshinsky transformation can be performed without problem. The usage of HO states, as intermediate states, when calculating matrix elements of a fully finite range interaction, has proven to be a very powerful tool for the GSM calculations. It gives us the freedom of using the most general interactions, without constraining their action mainly on the nuclear surface.

Parametrizations.

The SDI involves the energy cut-off and for that reason the contours extent from $\Re[k] = 0$ fm^{-1} to $\Re[k_{max}] = 2.6$ fm^{-1}. The $p_{3/2}$ contour is complex and consists of three segments defined by points: $k_1 = 0.0$, $k_2 = (0.17 - i0.15)$, $k_3 = (1.0 + i0.0)$ and $k_4 = (2.6 + i0.0)$, and it was discretized with a total of 30 points (shells), while for the rest partial waves we used 21 points (shells) each, resulting in a total of 115 s.p basis states. The same number of states was used for the SGI but in this case the maximum momentum of the s.p basis was chosen to be $\Re[k_{max}] = 3.27$ fm^{-1}. The parameters of both forces were fitted in order to reproduce the 0^+ g.s energy of ^{6}He. Additionally the quadruple strength of SGI to the excitation energy of the 2^+ first excited state of ^{6}He. The MN interaction, due its finite range, does not generate any cut-off dependence. We used the same contours as in the previous calculations

extending them up to k_{max}=4fm^{-1} and the force was renormalized by fitting the two Gaussian strengths to the g.s energy of ^{6}He and ^{8}He. The parameters that we adopted are: V_{0R}=+250.2MeV and V_{0s}=-110.1MeV.

2.2 Experimental Charge radii

Experimentally there exist many methods to extract charge distributions of nuclei. The one important in the context of this work include:

1. Electron scattering experiments.

2. Nuclear reaction cross sections and elastic proton scattering.

3. Atomic isotopic shift method.

In electron scattering experiments the charge radius of the system is extracted in a model independent way since it involves an electromagnetic probe (electrons). The charge radius is extracted from the Sachs $G_E(q^2)$ form factor (part of the differential cross section in the Rosenbluth formula) as:

$$\langle r_{ch}^2 \rangle = -6 \frac{dG_E(q^2)}{dq^2}|_{q^2=0}. \tag{2.16}$$

This method has been used for the determination of the charge radius for numerous heavy nuclei, and it was deduced that the charge radii are proportional to the $A^{1/3}$, as an indication of the nuclear matter saturation. For light systems electron scattering has been used to determine the charge radius of ^{3,4}He [84, 85]. The limitation of the method lies in the fact that it is not applicable to short lived nuclei such as ^{6,8}He.

For short lived nuclei a method that is commonly used is the scattering of radioactive beams on stable targets in inverse kinematics. The proton or neutron distributions are then extracted from the interaction cross sections in a model dependent way, since usually a Gaussian or Harmonic Oscillator distribution is assumed for the core and valence nucleons distribution [8].

During the last 4 years, measurements of isotopic shifts in atomic transitions determined the charge radii of halo nuclei ^{6}He [30], ^{8}He [31], ^{11}Li [86], and ^{11}Be [87] listed in Table 2.2. The basic advantage of these experiments is their high precision and also the fact that the charge radii are extracted from the measured isotopic shifts with the help of high precision atomic theory calculations, making this approach model-independent. The basic idea behind the isotopic shift measurements

Table 2.2: Rms charge radii of ^{6,8}He, ^{11}Li, and ^{11}Be measured in recent experiments.

Nucleus	Ref.	$\sqrt{\langle r_{ch}^2 \rangle}$ (fm)
^{6}He	[31]	2.068(11)
^{6}He	[30]	2.054(14)
^{8}He	[31]	1.929(26)
^{11}Li	[86]	2.467(37)
^{11}Be	[87]	2.463(16)

lies in the fact that when the "cloud" of electrons is inside the nucleus, the electrostatic Coulomb potential is changed. This is the screening effect that results in a reduced electromagnetic force between the electrons. As a consequence, this weakened interaction energy causes the energy levels to rise. Then by measuring the corresponding transition frequency the charge radius can be extracted. The formula that relates the charge radius with the frequency difference is given by [30]:

$$\delta\nu = -\frac{2\pi}{3} Z e^2 \Delta |\Psi(0)|^2 \delta \langle r_{ch}^2 \rangle \tag{2.17}$$

where the $\Delta|\Psi(0)|^2$ defines the difference of the electronic wave function inside the nucleus and can be calculated by high precision atomic theory calculation. The electronic levels can also be modified by varying the mass of the nucleus. Knowledge of the mass of the nucleus with the highest precision will result in a more accurate extraction of the charge radius. This was achieved very recently by Penning trap mass measurements which has resulted in a revaluation of the ^{6,8}He charge radii [11].

2.2.1 Factors that impact the charge radii of ^{6,8}He

In neutron halos, the charge radius can provide us with invaluable information about the dynamics of valence neutrons. The change in charge radius due to valence halo neutrons stems from two factors. The first is the motion of the core around the common center of mass, and the second is the monopole core polarization (or core "swelling"), due to the interaction between the halo nucleons and the core. To make contact with the measured charge radii, we correct the calculated point-proton radii for the finite sizes of proton and neutron through (2.18). We also consider the Darwin-Foldy (D.F) term and the effect of the spin-orbit (s.o) charge density which is discussed in [88].

$$\langle r_{ch}^2 \rangle = \langle r_{pp}^2 \rangle + \langle R_p^2 \rangle + \frac{N}{Z}\langle R_n^2 \rangle + \frac{3}{4M_p^2} + \langle r^2 \rangle_{so}. \tag{2.18}$$

In our work, we took the standard values of $\langle R_p^2 \rangle$=0.769 fm^2 (proton charge radius), $\langle R_n^2 \rangle$=-0.1161 fm^2 (neutron charge radius), and $\frac{3}{4M_p^2}$=0.033 fm^2 (Darwin-Foldy term). For the s.o charge density we use the explicit formulas from [88]. This density arises from a Foldy-Wouthuysen transformation which reduces the 4-component relativistic wavefunction into a non-relativistic form. It is worth mentioning that the Darwin-Foldy term in (2.18) is a product of this transformation as well. The physical content of the s.o. density is attributed to the interaction of the magnetic moment of the particle μ_i with the magnetic field in its rest frame. It has been shown that the s.o interaction can cause a significant change in the charge distribution [89] and its size was estimated recently in helium, lithium and beryllium nuclei [90]. To compute the s.o. contribution to the charge radius, we introduce the s.o density:

$$\rho_{so}(r) = -\frac{1}{r^2}\frac{d}{dr}(r\rho_{LS}(r)) \tag{2.19}$$

with

$$\rho_{LS} = \langle \Psi | \sum_i \left(\frac{2\hat{\mu}_i - \hat{e}_i}{4m^2} \right) \delta^3(\boldsymbol{r} - \boldsymbol{x}_i^{'}) \boldsymbol{\sigma}(i) \cdot \boldsymbol{L}_i | \Psi \rangle. \tag{2.20}$$

where $\boldsymbol{\sigma}$(i) is twice the spin of the ith particle, $\boldsymbol{L}$(i) its angular momentum, μ_i and e_i its magnetic moment and electric charge, respectively. The s.o. contribution to the charge radius is given by the integral:

$$\langle r^2 \rangle_{so} = \int r^2 \rho_{so}(r)\, dr. \tag{2.21}$$

In ^{6}He, the halo neutrons are spatially correlated and the recoil motion of the core results in an appreciable increase of the charge radius from the value of 1.68 fm in ^{4}He (see Table 2.2) [84]. On the other hand, while the charge radius of ^{8}He is larger than the one in ^{4}He, it is slightly smaller compared to r_{ch} in ^{6}He. This, at first sight, suggests that as the halo neutrons in ^{8}He are distributed more democratically around the core, so is the recoil motion smaller. It is interesting to mention that an additional geometry of the halo neutrons in ^{8}He has been predicted in recent *ab initio* quantum Monte Carlo calculations [91]. In this configuration the halo neutrons form a triangular pyramid around the α-core. The possible distribution of the halo neutrons in ^{6,8}He is shown in Fig.(2.3).

In spite of the fact that the α-core is tightly bound, quantum Monte Carlo calculations predict a small core polarization contribution to the charge radius [13]. This was demonstrated by inspecting the two-proton distribution density:

$$\rho_{pp}(r) = \frac{1}{4\pi r^2} \langle \Psi | \sum_{i<j} \frac{1-\tau_{zi}}{2} \frac{1-\tau_{zj}}{2} \delta(r - |\mathbf{r}_i - \mathbf{r}_j|) | \Psi \rangle \tag{2.22}$$

which is not sensitive to the CM motion. The theory predicts an 4.58% effect when going from ^{4}He to ^{6}He and about an 6.66% increase when going from ^{4}He to ^{8}He. Consequently, the "swelling" of the core cannot be neglected in the detailed analysis. In the calculations for ^{6}He we have thus adopted the value 1.527 fm for the point proton radius of α-core while for ^{8}He we are using the value 1.557 fm [92]. Similar arguments apply to the cases of ^{11}Be and ^{11}Li shown in Table 2.2. For reference,

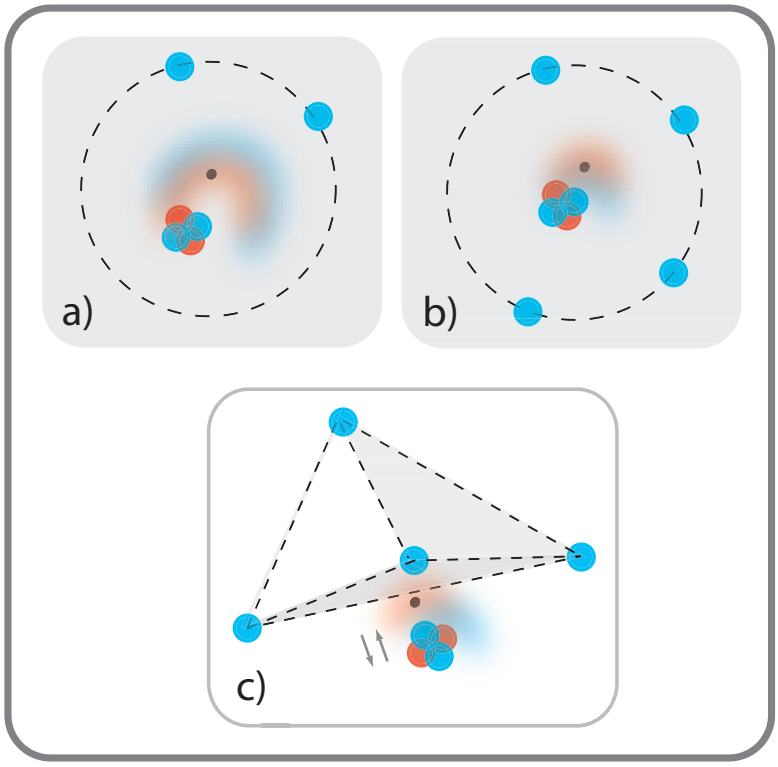


Figure 2.3: Possible geometries of halo neutrons with respect to the α core in ^{6}He (a) and ^{8}He (b and c).

the measured proton charge radii in the core nuclei ^{9}Li and ^{10}Be are 2.217 fm and 2.357 fm, respectively.

Chapter 3

Neutron correlations in ^{6,8}He nuclei

3.1 Neutron Correlations in ^{6}He nucleus

.

According to the measurements, the correlations of the valence neutrons in ^{6,8}He are essential for the understanding of the charge radii differences. Before discussing GSM predictions for the charge and neutron radii, we present results for the 2n correlations. The force that we employ for this study was the Modified Minnesota (MMN) interaction. We call it Modified Minnesota Interaction (MMN) since-as we discussed earlier-we modify the strengths of the Gaussian form factors of the initial Minnesota force. By fitting the force to the g.s energies of ^{6,8}He we also predict

Table 3.1: GSM Hamiltonian eigenvalues for the g.s of ^{6}He and some excited states. The values are in MeV. Experimental data are taken from [1]. Energies are expressed in the form E = E_r - i$\frac{\Gamma}{2}$, where Γ is the width.

	GSM	Experiment
0^+_1	-0.975	-0.975
0^+_2	3.897 - i3.17	—
2^+_1	0.851 - i0.0545	0.822(25) - i0.0565(20)
2^+_2	5.234 - i3.825	—

that the first excited 2^+ state of ^{6}He is in close agreement with experiment, see Table 3.1. Also the predicted $3/2^-$ g.s. resonance of ^{7}He has $E = -0.707$ MeV

($E_{exp} = -0.528\,\mathrm{MeV}$). Consequently the current GSM parametrization reproduces the energetics of the isotopic chain $^{5-8}$He, in particular the one-neutron (1n) and two-neutron (2n) thresholds. The particle correlations in Halo nuclei were studied in

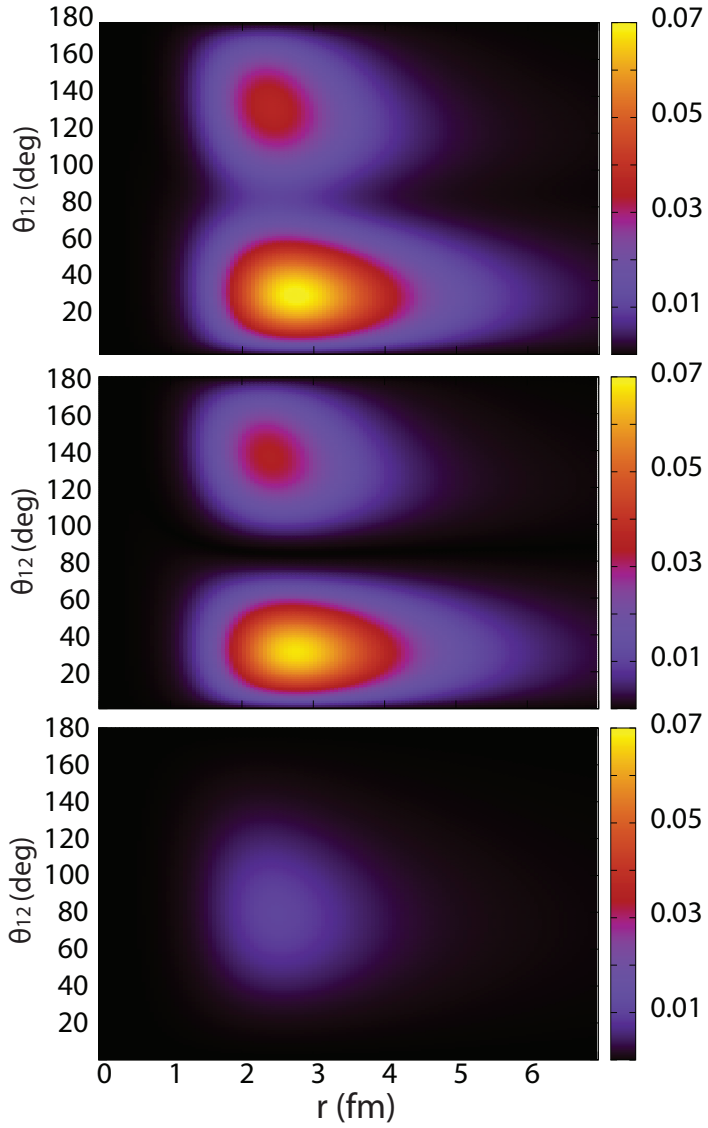


Figure 3.1: Contour plots of the two body correlation density in ^{6}He. In the upper panel is shown the total correlation, while the middle and bottom show the S=0 and S=1 components respectively. Notice the radial tail of the S = 0 component.

a series of publications [93, 94, 95, 76, 96, 97, 98, 99] by treating the nucleus as a three-body cluster. On the experimental side the particle correlations have been studied by investigating their effect on the reaction cross section of transfer reactions [100]

and also by using techniques of intensity interferometry in dissociation experiments [101, 102]. The main strategy that is followed in theory in order to assess these correlations is the calculation of the two body correlation density. In the COSM coordinates we can parametrize the wavefunction in a form that we would be able to make a detailed analysis of the geometric form of the nuclear states. In our case we define the correlation density as:

$$\rho(r_1, r_2, \theta_{12}) = \langle \Psi | \delta(r_1 - r)\delta(r_2 - r')\delta(\theta_{12} - \theta) | \Psi \rangle \tag{3.1}$$

where r_1,r_2 and θ_{12} are defined in Fig.2.2. In the LS coupling scheme the general non-antisymmetrized matrix element of the operator (for brevity we neglect the exchange part):

$$O = \delta(r_1 - r)\delta(r_2 - r')\delta(\theta_{12} - \theta)$$

is given by:

$$\begin{aligned}
&\langle \psi^{(\alpha)}(\alpha_1, \alpha_2, \mathbf{r}_1, \mathbf{r}_2) | \hat{O} | \psi^{(\alpha)}(\alpha_1, \alpha_2, \mathbf{r}_1, \mathbf{r}_2) = \\
&\quad N(\alpha_1, \alpha_2) N(\alpha_1', \alpha_2') \sum_{\lambda, S} \gamma_{\lambda,S}(j_a, l_a, j_b, l_b) \gamma_{\lambda,S}(j_c, l_c, j_d, l_d) \\
&\quad r^2 r'^2 \phi_{n_a l_a j_a}(r) \phi_{n_b l_b j_b}(r') \phi_{n_c l_c j_c}(r) \phi_{n_d l_d j_d}(r') \\
&\quad \sin(\theta) W^{\lambda}_{l_a l_b l_c l_d}(\cos\theta),
\end{aligned} \tag{3.2}$$

where the N(α_1, α_2) are normalization coefficients, $\psi^{\alpha}(\alpha_1, \alpha_2, \mathbf{x}_1, \mathbf{x}_2)$ are the two-body normalized antisymmetrized basis functions which are expressed in the LS coupling scheme, and

$$\gamma_{\lambda,S}(j_a, l_a, j_b, l_b) = \hat{j_a}\hat{j_b}\hat{\lambda}\hat{S} \begin{Bmatrix} l_a & \frac{1}{2} & j_a \\ l_b & \frac{1}{2} & j_b \\ \lambda & S & J \end{Bmatrix}$$

is the coefficient for the jj-LS transformation and $\hat{x} = \sqrt{2x+1}$. The W function is defined as [103]:

$$W^{\lambda}_{l_a l_b l_c l_d} = \frac{1}{2}(-1)^{\lambda}\hat{l_a}\hat{l_b}\hat{l_c}\hat{l_d}\sum_{L}(-1)^{L}(2L+1) \\ \begin{pmatrix} l_a & l_c & L \\ 0 & 0 & 0 \end{pmatrix} \begin{pmatrix} l_b & l_d & L \\ 0 & 0 & 0 \end{pmatrix} \begin{Bmatrix} l_c & l_d & \lambda \\ l_b & l_d & L \end{Bmatrix} P_{L0}(\cos\theta) \tag{3.3}$$

and $\phi_{nlj}(r)$ denotes the radial Gamow basis wave-function. In a forthcoming publication we will present a detailed derivation of (3.2) in a context of comparing energetics and radial properties of the GSM with the Complex Scaling method in a Slater Orbital basis [79]. The expression of the correlation density in the LS coupling scheme has the advantage that one can readily split it into the S=0 and S=1 components and see which component has the dominant contribution. In that way we obtain a deeper insight of the spatial structure of the wave-function. The definition in (3.2) is valid not only for ground states, but also for excited states. The correlation density satisfies the normalization condition:

$$\int dr_1 \int dr_2 \int_0^{\pi} \rho(r_1, r_2, \theta_{12})\, d\theta_{12} = 1. \tag{3.4}$$

In Fig.3.1 we plot the correlation density for $r_1 = r_2 = r$ as a function of r and θ. The calculations were performed in the p-sd shell with the MMN force of Chapter 4.3. We see that the total density is characterized by two peaks. The one that corresponds to small angles is usually referred to as di-nucleon configuration, in which the valence neutrons reside very close to each other, while the one in larger angles is known as cigarlike configuration where the neutrons move on opposite sides of the α-core. The di-nucleon peak is not only more pronounced, but it is spatially extended, suggesting that the two neutrons exist most of the time very close to each other and also in a large distance (halo) from the core. This behavior verifies the scenario of the charge

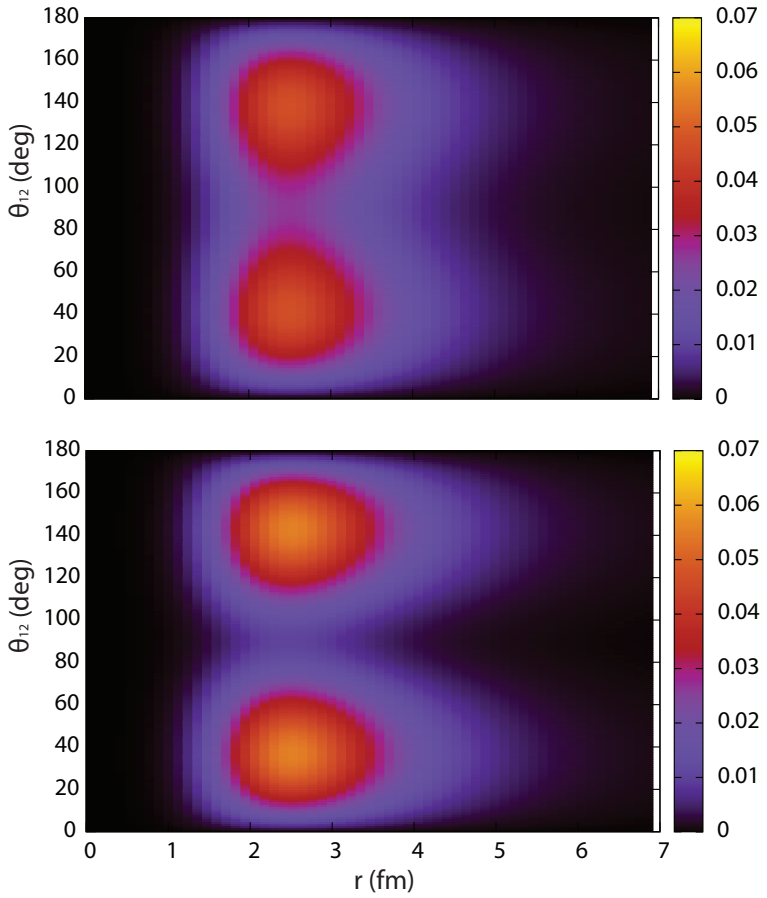


Figure 3.2: Contour plots of the two body correlation density in ^{6}He. In the top panel is shown the correlation density when the two-body interaction is switched off, while in the bottom panel we use a MMN interaction in a restricted p-shell model space

radius increase in ^{6}He. The cigarlike configuration on the other hand is less probable and more confined radially. It is worth noting that these configurations were also confirmed experimentally by their contribution to the cross section of two-neutron transfer reactions [100].

By inspecting the middle and bottom panel of Fig.3.1 we see that the ^{6}He g.s is dominated by the S=0 configuration. Integrating the S=0 and S=1 parts of the correlation density we can have an idea of the weights of these configurations. For the S=0 we find an 87.3% concentration and for the S=1 an 12.7%. Hence, one of the origins of this two-component structure in ^{6}He is related to the S=0 dominating

configuration in the g.s wave-function. Additionally, it was found in [104] that the Pauli principle is very important for the existence of the two aforementioned particle correlations. Our calculations verify that if the Pauli Principle, that forbids the valence neutrons to occupy the $0s_{1/2}$, is not taken into account, the two peaks in the correlation are smeared out. This effect is known in the few-body community as "Pauli focusing" effect.

To investigate further the details of the spatial the structure of the ^{6}He wavefunction we turn off the two-body interaction. This gives results presented in the top panel of Fig.3.2. The two peak structure appears again, but now the di-nucleon configuration is weakened and the peaks acquire the same height. Also the halo feature in the density distribution has been decreased considerably. In the lower panel we make a calculation with the two-body interaction present but restricting ourselves in a full p-shell only. The situation is slightly changed but the two configurations have the same height and the di-nucleon structure is not enhanced. This leads to the conclusion that the necessary condition for an enhanced di-nucleon structure in ^{6}He is, the presence of the two-body a interaction, and more importantly the model space containing partial waves of mixed parity. Quantitatively we understand this behavior if we analyze the angular dependence of the correlation function in a model space of a $p_{3/2}$* wave only. From (3.3) we obtain by using the numerical values of the Wigner symbols, that the S = 0 component is proportional to:

$$\rho(r,\theta_{12}) \propto \frac{1}{3}P_{00}(\cos\theta_{12})\sin\theta_{12} + \frac{2}{3}P_{20}(\cos\theta_{12})\sin\theta_{12} \tag{3.5}$$

and the S = 1 component is proportional to:

$$\rho(r,\theta_{12}) \propto \frac{1}{18}P_{00}(\cos\theta_{12})\sin\theta_{12} - \frac{1}{18}P_{20}(\cos\theta_{12})\sin\theta_{12} \tag{3.6}$$

*When the two-body interaction is switched off, no configuration mixing is induced and the wavefunction is characterized by a single $C^2_{p_{3/2}} = 1$ amplitude

where

$$P_{L0}(\cos\theta) = \sqrt{\frac{4\pi}{2L+1}} Y_{L0}(\theta_{12}). \tag{3.7}$$

This yields: $\rho^{S=0}(r,\theta_{12}) \propto \sin\theta_{12}\cos^2\theta_{12}$ and $\rho^{S=1}(r,\theta_{12}) \propto \frac{1}{12}\sin^3\theta_{12}$. Indeed, in the interval of $\theta\,\epsilon\,[0,\pi]$ the first function has two equal maxima at smaller and larger angles while the latter has one maximum at 90^o. By switching on the two-body

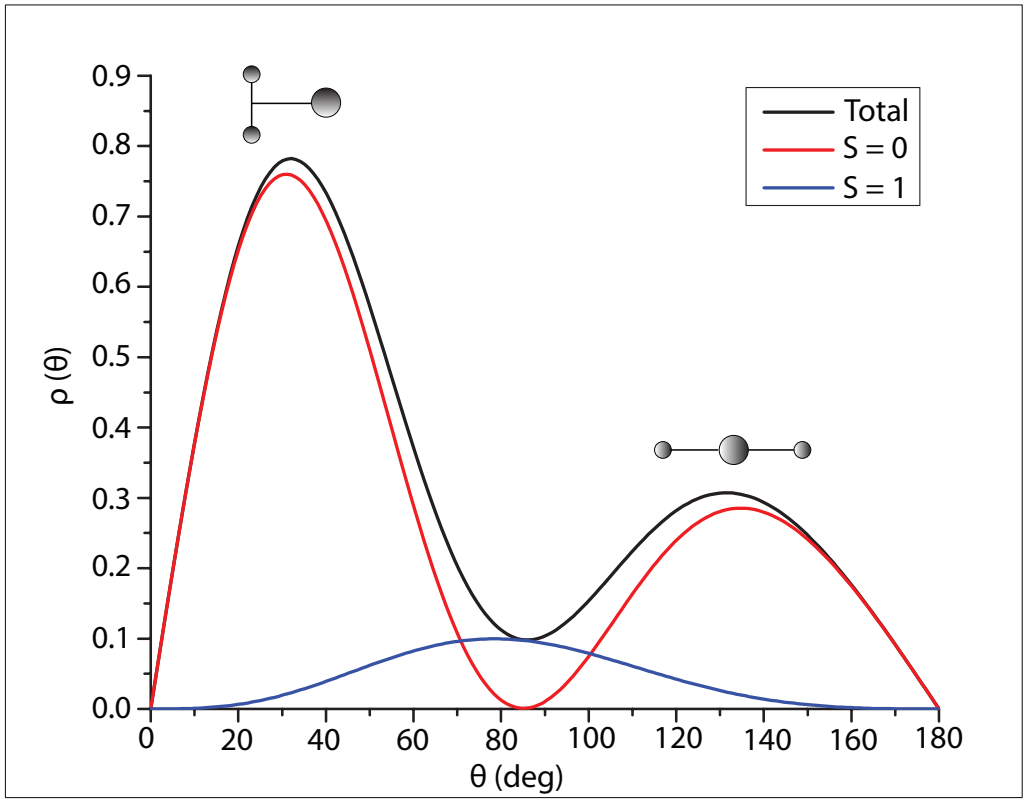


Figure 3.3: Angular densities of the ^{6}He g.s.

interaction and adding more partial waves this picture is changed, see (Fig.3.1). This clusterization is a manifestation of the continuum coupling which is treated exactly within the GSM. The enhancement of the di-nucleon configuration when we use a

Table 3.2: Impact of the model space on the rms charge radius of ^{6}He

Model space[†]	$\sqrt{\langle r_{ch}^2 \rangle}$ (fm)
p-shell	1.898
p-sd shell	2.026

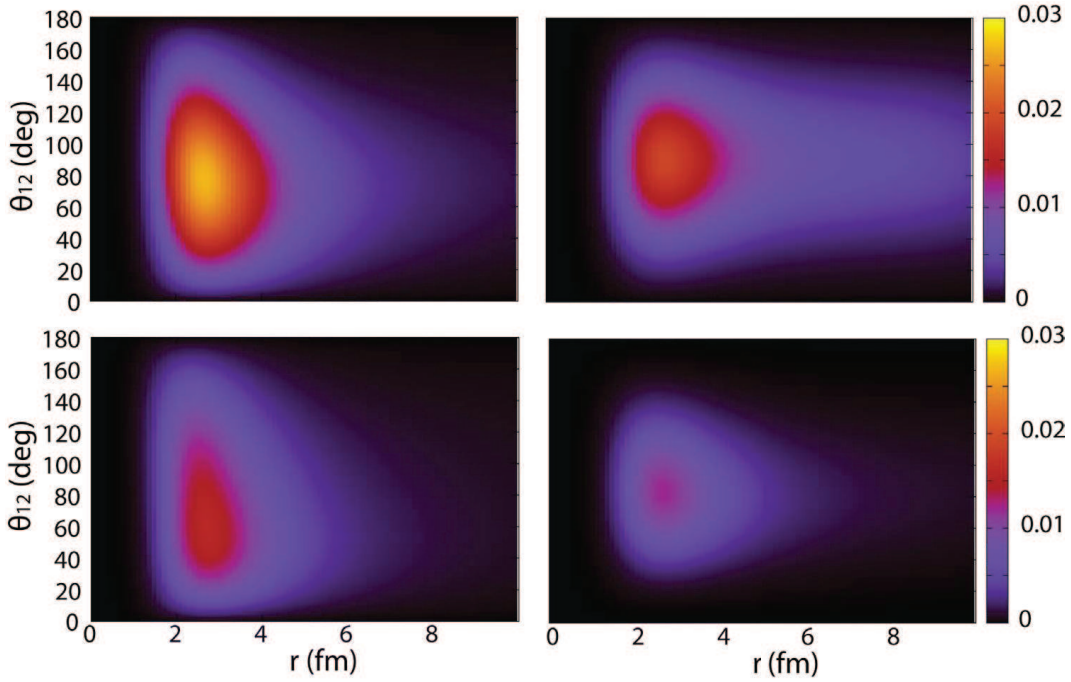


Figure 3.4: Correlation density of the 2^+ state of ^{6}He. The left top panel shows the total density, while the left and right bottom the S=0 and 1 channels respectively. In the right top panel we present the correlation density when the two-body interaction is turned off. The calculation is performed in a p-sd model space.

p-sd space has a pronounced effect on the rms charge radius, since in the latter case the recoil motion of the core is larger (see Table 3.2). We continue the discussion on the geometry of the ^{6}He g.s wavefunction by introducing the angular density. This quantity is derived by the integration of the r_1 and r_2 coordinates of the correlation function $\rho(r_1, r_2, \theta_{12})$:

$$\rho(\theta_{12}) = \int dr_1 \int dr_2 \rho(r_1, r_2, \theta_{12}) \tag{3.8}$$

With this density the average opening angle is found to be $\theta_{nn} = 68.1^o$ in accordance with (4.5). It is now transparent that the average opening angle results from an average of a smaller and larger angle (di-nucleon/cigarlike) probabilities in the density

distribution (Fig.3.3). The neutrons are possible to be found in both geometries but most of the time are coupled together in the one side of the nucleus, that is why the opening angle is close to 70^o. Also, the dominance of the S=0 part is clearly seen more. To conclude, after performing similar calculations with other forces we realized that these configurations do not depend on the details of the two-body interactions. That is the reason the results on rms radii and correlation angle, using three different interactions, are very close to each other.

Next, we discuss the neutron correlations in the first excited state of ^{6}He which is embedded in the continuum (Table 3.1). In Fig.3.4 we plot the correlation density of the 2^+ state as a function of r and θ. The two-body density is radially extended, reflecting the unbound character of the 2^+ state, and it is characterized by one peak, contrary to the 0^+ state. We find that the weight of the S=0 configuration is 66.2% and 33.8% for the S=1. We next switch off the two-body interaction and the results are shown in Fig.3.4 (right top panel). The effect of the absence of the interaction is small on the form of the two-body density and the basic feature of the one peak is unaltered. By inserting in (3.3) the values of the Wigner symbols for the case of a $p_{3/2}$ wave, we find that the S=0 component is proportional to:

$$\rho(r,\theta_{12}) \propto \frac{1}{6}P_{00}(\cos\theta_{12})\sin\theta_{12} + \frac{1}{30}P_{20}(\cos\theta_{12})\sin\theta_{12} \tag{3.9}$$

and the S=1 component is proportional to:

$$\rho(r,\theta_{12}) \propto \frac{1}{12}P_{00}(\cos\theta_{12})\sin\theta_{12} - \frac{1}{12}P_{20}(\cos\theta_{12})\sin\theta_{12} \tag{3.10}$$

Using the values for the Legendre polynomial through (3.7) we find that $\rho(r,\theta_{12}) \propto \frac{3}{20}\sin\theta_{12} + \frac{1}{20}\cos^2\theta_{12}\sin\theta_{12}$ for the S=0 and $\rho(r,\theta_{12}) \propto \frac{3}{24}\sin^3\theta_{12}$ for the S=1. The first equation has a maximum at $\theta_{12} = 90^o$ and is characterized by a small plateau around 90^o, while the second has a narrow maximum at 90^o. This is indeed the situation for the 2^+ state of ^{6}He. By inspecting Fig.3.4 we see that the interaction

and the induced configuration mixing of the p-sd waves does not affect considerably the spatial characteristics of the wavefunction of the 2^+ state. This is an indication that the valence neutrons in the first excited state of ^{6}He are almost uncorrelated. In Fig.3.5 we show the corresponding angular density. In the case of switching off the interaction the average opening angle of the neutrons in the 2^+ is $\langle\theta_{nn}\rangle = 90^o$, while when the interaction is present we find that: $\langle\theta_{nn}\rangle = 82.6^o$, as it can be deduced

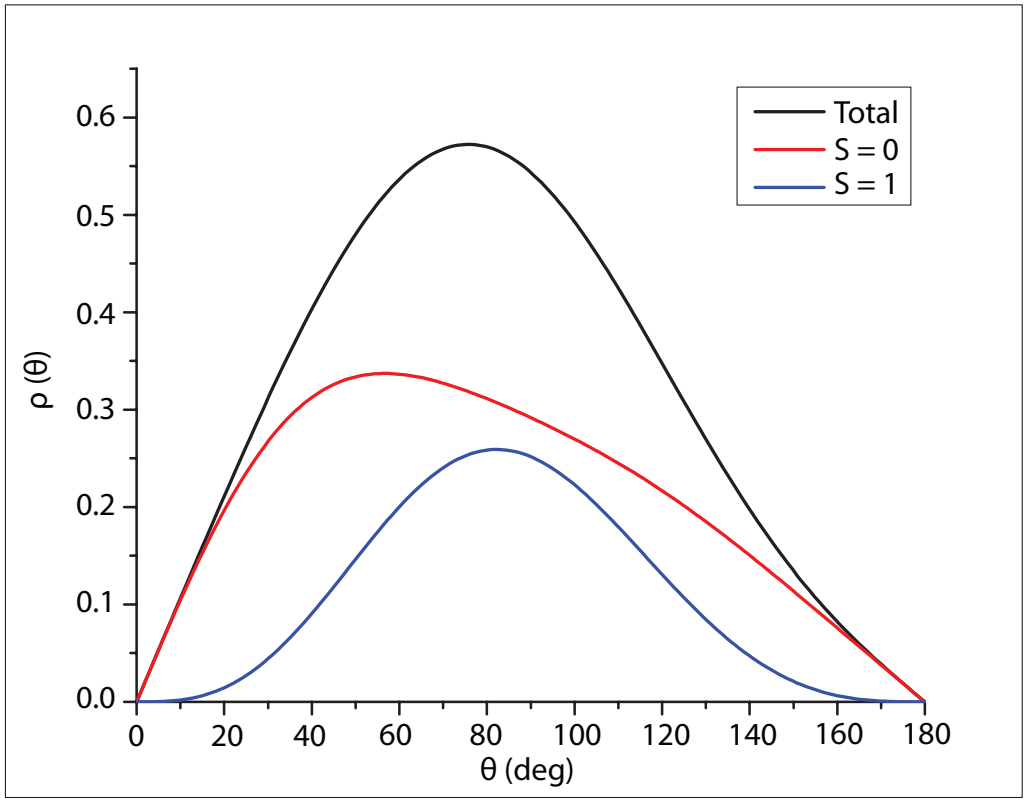


Figure 3.5: Angular densities of the ^{6}He 2^+ excited state.

from the angular density distribution. We see that the interaction causes a very small deviation from 90^o which agrees with the scenario of uncorrelated neutrons in the 2^+ state. The expectation value of an operator $\hat{O}$ in a resonant state is given by the real part $\langle\hat{O}\rangle = \Re\langle\Psi|\hat{O}|\Psi\rangle$. The imaginary part is associated with the uncertainty of the mean value. For the angle the uncertainty is: $(\Delta\theta)^2 = 3.3^o$.

Contrary to the ^{6}He 0^+ g.s where similar results were obtained by several authors, the correlations in the 2^+ state are probed for first time in this work. We found

a publication [94] where the two-body density of the excited 3^+ state of ^{6}Li was calculated and it is characterized by one peak as well.

3.2 Neutron Correlations in ^{8}He nucleus

.

We next study the neutron correlations in g.s. of ^{8}He. As we see in Fig.(3.6) the situation is very similar to the ^{6}He ground state case. Nevertheless, some subtle

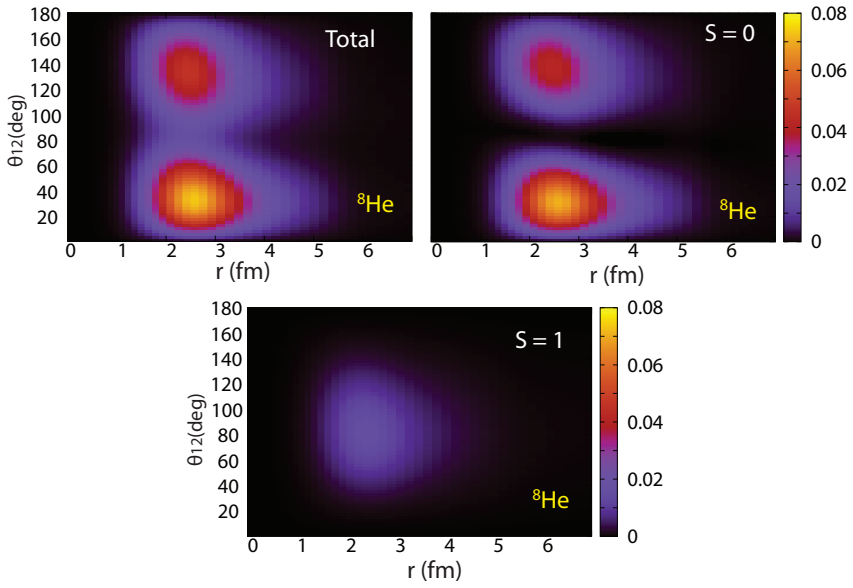


Figure 3.6: Correlation densities of the ^{8}He 0^+ excited state.

differences can be noticed, such as the fact that the radial extent is reduced in the ^{8}He nucleus. This is related to its larger binding energy. To get a better insight on the differences in correlations between ^{6,8}He we compare the angular correlations of both systems in Fig.(3.7). Our calculations demonstrate that the weight of the dineutron structure in ^{8}He is less than in ^{6}He due to increased strengths of cigar-like and $S = 1$ components. The addition of the two extra neutrons results in a slight increase in the average opening angle from $\theta_{12} = 68°$ in ^{6}He to $\theta_{12} = 78°$ in ^{8}He. It is worth noting, however, that the positions of the two peaks in $\rho_{nn}(\theta_{12})$ are practically the same in ^{6,8}He, and the 2n correlation density does not broaden up (i.e., becomes more

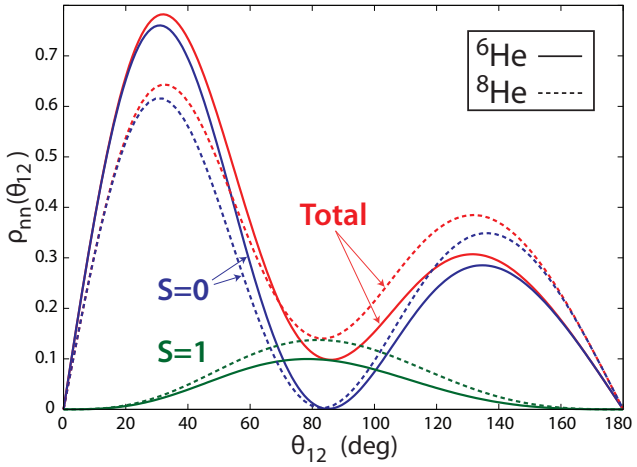


Figure 3.7: Angular 2n GSM densities (S=0, 1, and total) for g.s. configurations of ^{6}He (solid lines) and ^{8}He (dashed lines).

"democratic") in ^{8}He. We conclude that this reduction of the di-neutron component is one of the reasons behind the decrease of the charge radius of ^{8}He with respect to ^{6}He. The correlations of neutrons in ^{8}He are such that they decrease the orbital motion of the core around the common nuclear center of mass, resulting in the reduction of the charge radius.

Chapter 4

GSM calculations for ^{6,8}He nuclei

4.1 Radii operators and computation of radial integrals

After discussing neutron correlations in ^{6,8}He we are ready to calculate the charge and neutron radii. In the following, we are presenting the expressions needed to compute the charge and neutron radius. In the COSM coordinates of Fig.(2.2) the point proton radius is defined as:

$$\langle r^2_{pp}(^6\text{He})\rangle = \langle r^2_{pp}(^4\text{He})\rangle + \frac{1}{A^2}\langle r_1^2 + r_2^2 + 2\mathbf{r}_1\cdot\mathbf{r}_2\rangle, \tag{4.1}$$

where the first term denotes the point proton radius of the α-core, and the second term takes into account the recoil motion of the core. The generalization of this formula to heavier systems is straightforward, and we find that for the n valence neutrons, the point proton radius is given by:

$$\langle r^2_{pp}(^{A_c+n}X)\rangle = \langle r^2_{pp}(^{A_c}X)\rangle + \frac{1}{(A_c+n)^2}\sum_{i=1}^{n}\langle r_i^2\rangle + \frac{2}{(A_c+n)^2}\sum_{i<j}^{n}\langle \mathbf{r}_i\cdot\mathbf{r}_j\rangle \tag{4.2}$$

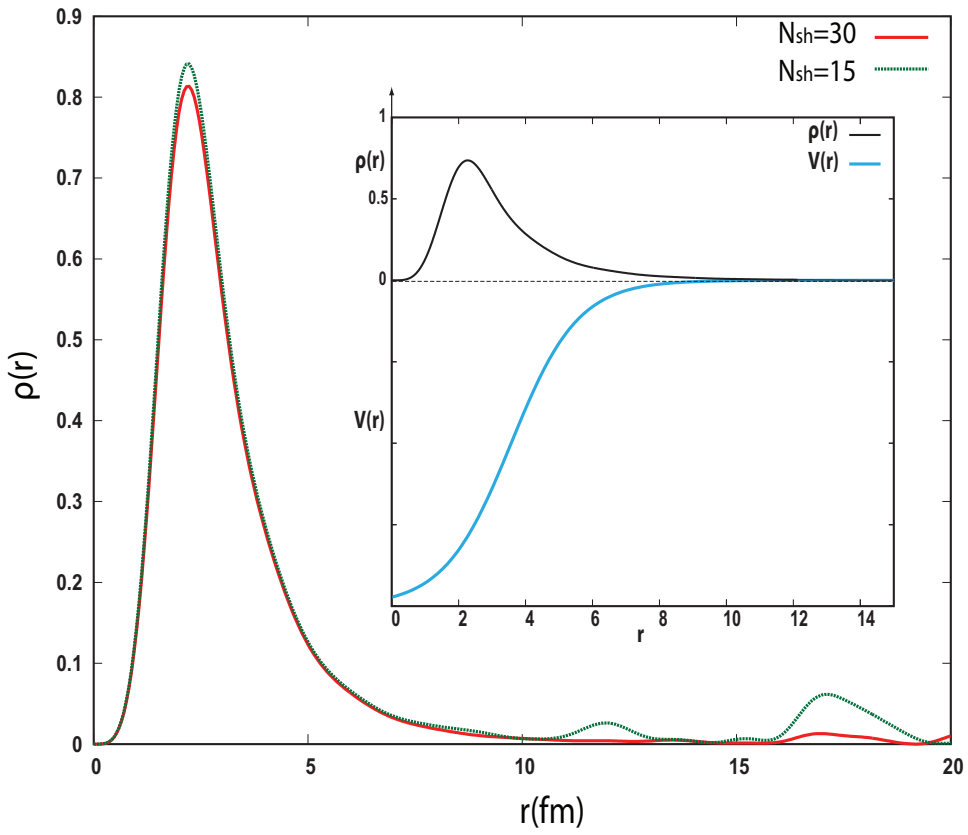


Figure 4.1: Radial halo density of ^{6}He calculated in GSM with **SGI** interaction. Since ^{6}He is a bound system, its valence neutrons are localized in space. Consequently, the integral (4.4a) involving the r^2 operator can be cut around 20 fm. The inset shows the radial density together with the radial form factor of the s.p. WS potential used to generate the Berggren basis. The number of contour discretization points N_{sh} is indicated.

where the core nucleus is ^{A_c}X. Notice that for $A_c \to \infty$ the second term disappears and the charge radius of the Helium isotopes becomes equal to the charge radius of the α-core. This argument shows that this operator is an estimate of the orbital motion ("recoil") of the core around the nuclear CoM. Similar formulas are derived for the neutron radius:

$$\langle r_n^2(^6\mathrm{He})\rangle = \frac{1}{2}\langle r_n^2(^4\mathrm{He})\rangle + \frac{1}{4}\langle r_1^2 + r_2^2\rangle - \frac{(A-2)}{2A^2}\langle r_1^2 + r_2^2 + 2\mathbf{r}_1\cdot\mathbf{r}_2\rangle \tag{4.3}$$

for ^{6}He and for generalization to N-particles we refer the reader to [77]. To compute r_{pp}, we need to calculate matrix elements $\langle a|r^2|b\rangle$ and $\langle a|r_1|c\rangle\langle b|r_2|d\rangle$ that involve integrals of the form:

$$\int_0^\infty u_a(r) r^2 u_b(r)\, dr, \tag{4.4a}$$

$$\int_0^\infty u_a(r) r u_c(r)\, dr. \tag{4.4b}$$

When $|\alpha\rangle$ and $|\beta\rangle$ are scattering states, the integral (4.4a) needs to be regularized. Unfortunately, for the reasons given above, this cannot be done by means of the complex scaling. As illustrated in Fig.(4.1), the way of regularization comes from the fact that the two-neutron wave function of ^{6}He corresponds to a bound state. As seen in Fig.(4.1), by increasing the number of points along the contour, the fluctuations of the radial form factor at large distances become very small; this demonstrates that the Berggren completeness relation is well fulfilled. In practice, with $N_{sh}\sim$45 discretization points, the fluctuations are smeared out, and it is safe to carry out the integration up to a certain cut-off radius. The stability of the results was checked by varying the cut-off radius $R_{\rm cut}$ and noting that with N_{sh}=45, the radial integral is practically unchanged for $R_{\rm cut}$ in the range [15,30] fm. In our calculations the cut-off radius was chosen to be $R_{\rm cut}$=20 fm.

4.2 Calculations with schematic forces

We begin the discussion by considering the SDI and SGI as a residual interactions. Initially we varied only the strength of the forces, keeping the surface parameter $R_0 = 2fm$ and we noticed that the point-proton radius of ^{6}He is relatively small. We proceeded by modifying also R_0 and the results are summarized in Table 4.1. The strength parameter for $R_0 = 4.4$fm was found to be $V_{SDI} = -2200.0\,\text{MeV}\cdot\text{fm}^3$ in order to reproduce the 0^+ g.s energy while for the SGI the obtained values for the strengths at $R_0 = 3.1$fm, are: $V_{J=0,T=1} = -387.6$MeV and $V_{J=2,T=1} = -556$MeV.

We observe a gradual increase of the point-proton radius when we force the particles to interact at larger distances. This is what is expected, since the further from the center of the nucleus the particles are interacting, the further the CoM of the whole system is shifted from the center of the nucleus, giving rise to an enhanced charge distribution. In order to compare our predictions with experiment, we convert the point-proton radius to charge radius according to (2.18). The effect of the s.o charge density on the mean square radius is found to be:

$$\langle r^2 \rangle_{so} = \int r^2 \rho_{so}(r)\, dr = -0.0713\text{fm}^2.$$

for SDI and

$$\langle r^2 \rangle_{so} = \int r^2 \rho_{so}(r)\, dr = -0.0743\text{fm}^2.$$

for SGI. Together with the s.o correction we take into account the polarization of the. We cannot calculate this effect microscopically with our model, we use the results of the state of the art quantum Monte Carlo calculations that predict a $\sim 4\%$ increase of the ^{4}He charge radius as we discussed in Section 2.2. For the SDI we obtain that:

$$\sqrt{\langle r_{ch}^2 \rangle} = 2.056\text{fm}.$$

while for the SGI:

$$\sqrt{\langle r_{ch}^2 \rangle} = 2.049\text{fm}.$$

In Table 4.2 the weights of the several components of the wavefunction are presented.

Another important quantity, especially for the determination of the geometry of a Borromean system, is the correlation angle θ_{nn} between the valence neutrons (see also Fig.(2.2)). We can deduce this value from the relation:

$$\theta_{nn} = \arccos\left(\frac{\langle \mathbf{r}_1 \cdot \mathbf{r}_2 \rangle}{\langle |\mathbf{r}_1| \rangle \cdot \langle |\mathbf{r}_2| \rangle}\right). \tag{4.5}$$

Table 4.1: Point-proton radius of ^{6}He for different values of the surface parameter R_0 of SDI and SGI. All values are in fm.

SDI	
R0	$\sqrt{\langle r_{pp}^2 \rangle}$
2.0	1.65
3.0	1.716
4.0	1.806
4.4	1.885
SGI	
R0	$\sqrt{\langle r_{pp}^2 \rangle}$
2.0	1.784
2.5	1.808
3.1	1.879

We found that $\theta_{nn} = 65.2^o$ and $\theta_{nn} = 65.8^o$ for the SDI and SGI respectively. This result is similar to the previous estimates [105, 106] in which θ_{nn} was extracted from the strength of the B(E1) Coulomb dissociation rate.

Table 4.2: Decomposition of the ^{6}He g.s wavefunction with schematic forces.

	C_α^2	
	SDI	SGI
$(0p_{3/2})^2$	(0.703, -0.662)	(0.838, -0.721)
$(p_{3/2})^1_{scat}(0p_{3/2})^1$	(0.257, 0.587)	(0.128, 0.703)
$(p_{3/2})^2_{scat}$	(-0.0429, 0.0745)	(-0.0844, 0.0185)
$(p_{1/2})^2_{scat}$	0.048	0.042
$(s_{1/2})^2_{scat}$	0.0018	0.0086
$(d_{5/2})^2_{scat}$	0.022	0.055
$(d_{3/2})^2_{scat}$	0.009	0.011

4.3 Calculations with the Modified Minnesota Interaction

4.3.1 ^{6}He nucleus

In this section we use a MMN force which has neither a zero range nor peaks at the nuclear surface. The calculated s.o rms radius is found to be:

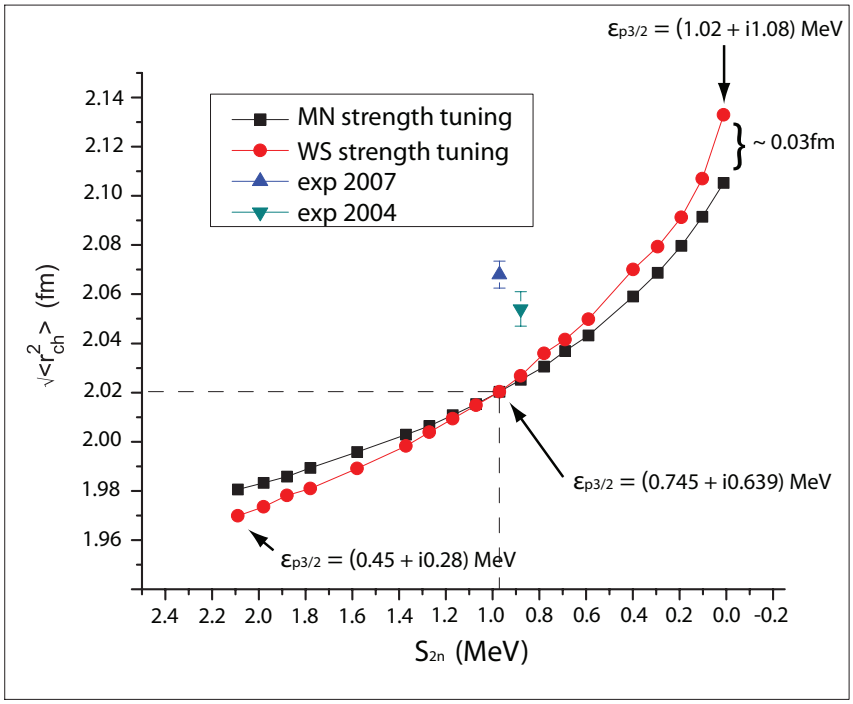


Figure 4.2: Evolution of the rms charge radius of ^{6}He as a function of the two-neutron separation energy for the MMN force. The two different curves correspond to i) changing the MMN strength (black) and ii) changing the WS strength (red). See text for details. The experimental values are included for comparison.

$$\langle r^2 \rangle_{so} = \int r^2 \rho_{so}(r)\, dr = -0.0718\text{fm}^2.$$

and including the polarization of the core, the rms charge radius is:

$$\sqrt{\langle r_{ch}^2 \rangle} = 2.026\text{fm}, .$$

which is very close to the measured one. The average angle between the neutrons is $\theta_{nn} = 68.11^o$ which is consistent with the two previous estimates using schematic forces. Table 4.3 summarizes the MMN wavefunction decomposition that the MMN force generates. In Fig.4.2 we vary the two-neutron separation energy (S_{2n}) by either

Table 4.3: Decomposition of the ^{6}He wavefunction obtained with the MMN force.

$(0p_{3/2})^2$	(1.03742, -0.741)
$(p_{3/2})^1_{scat}(0p_{3/2})^1$	(-0.100, 0.764)
$(p_{3/2})^2_{scat}$	(-0.057, -0.023)
$(p_{1/2})^2_{scat}$	0.049
$(s_{1/2})^2_{scat}$	0.021
$(d_{5/2})^2_{scat}$	0.0402
$(d_{3/2})^2_{scat}$	0.0089

modifying the singlet strength of the MMN interaction (black) or the WS depth (red) and we plot the rms charge radius as a function of this energy. The dependence of the charge radius while modifying the s.p potential is discussed in detail in Section (4.4).

We observe that when the system becomes more bound the charge radius is decreased and vice versa, for a less bound system. This is a consequence of the fact that when the system is more bound it is more confined and localized. The plot highlights the sensitivity of the results on S_{2n} of the halo nucleus. Additionally, by inspecting Table 4.3 (and also Table 4.2) we see that when S_{2n} of the system is reproduced the two-body wavefunction contains an $\sim$ 90% of $p_{3/2}$ occupation and-at the same time-states with angular momentum larger than one (d-waves) are suppressed. This is the case for the other interactions employed until now (SDI,SGI) and we believe that the $p_{3/2}$ occupation-together with the S_{2n}-is an important quantity for the determination of the ^{6}He point-proton radius. We conclude that the charge radius measurements favor a model with an $\sim$90% occupation of a $p_{3/2}$ component in the g.s of the ^{6}He. This kind of halo phenomenology has been used in the last 12 years, especially for ^{11}Li [107, 108, 109]. The 90% occupation of the $p_{3/2}$ orbit in ^{6}He is also confirmed by [58] and a recent three body model calculation estimated it to be

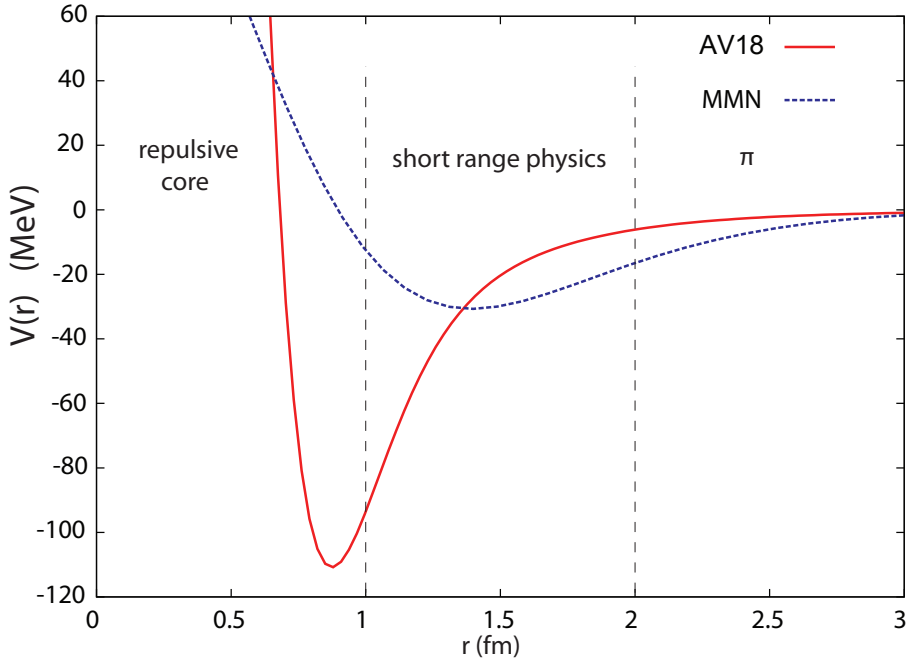


Figure 4.3: Comparison between the realistic AV18 force and the MMN used in this work. With π is denoted the one-pion exchange region.

83% [97]. Also, we found in the literature a calculation of Cohen and Kurath where they estimated the $p_{3/2}$ occupation of ^{6}He in a p-shell model space to be $\sim$95% [110].

Any interaction that reproduces the S_{2n} of ^{6}He is expected to give a satisfactory result with the charge radius measurement. The latter finding is consistent with GFMC calculations [10] that are using realistic two-body interactions plus three-body interactions. It was found that only when the separation energy was reproduced their charge radius was in agreement with the measurement [10]. The quantity one needs to control is S_{2n}, since this quantity describes the halo and the correlations of the particles (PAH effect). Halo nuclei are dilute systems, where the particles are spatially decoupled from the core, exhibit universal properties and mainly depend on the particle emission thresholds. In Fig.4.3 we present a comparison between a realistic force with a hard core (AV18) and the MMN. Both forces exhibit very different behavior at short distances, but for the description of the halo, the asymptotic region

is of primary importance. This is the basic reason that the description of halo nuclei does not depend on subtle details of the nuclear interaction.

4.4 Pairing "anti-halo" effect in ^{6}He.

To this end we are investigating the impact of the continuum on the many-body correlations, such as pairing. It is well know [111, 21, 112, 113, 114, 115, 116] that in the vicinity of particle threshold the pairing correlations are strongly affected. One example is the Pairing-Anti Halo (PAH) effect in which the continuum coupling generates an additional pairing binding energy, preventing the weakly bound system from developing an infinite radius. In the simple HF picture, where the pairing is not present, the wave function behaves asymptotically as (we assume an s-wave in the following):

$$\psi(r) \sim exp(-\kappa r) \tag{4.6}$$

with $\kappa = \sqrt{\frac{2m\epsilon}{\hbar^2}}$ and ϵ being the energy of the state. It turns out that the corresponding mean square radius behaves as:

$$\langle r^2 \rangle \sim \frac{1}{\epsilon} \tag{4.7}$$

and it shoots to infinity as ϵ approaches zero binding *. In the HFB framework where the pairing correlations are present, the asymptotic behavior of the wavefunction is dictated by the quasi-particle energy. This is given approximately (BCS) by:

$$E = \sqrt{(\epsilon - \lambda)^2 + \Delta^2} \tag{4.8}$$

and for $\epsilon \to \infty$ the mean square radius of the state is proportional to:

$$\langle r^2 \rangle_{HFB} \sim \frac{1}{\Delta} \tag{4.9}$$

*The square radius explodes for ℓ =1 waves as well [117]

The system stays localized because the pairing correlations expressed through the pairing gap prevent its rapid growth when the threshold is approached.

In the GSM we cannot separate the pairing contribution $\langle\Delta\rangle$ to the total energy. However one can implicitly identify the effect of the continuum on the pairing

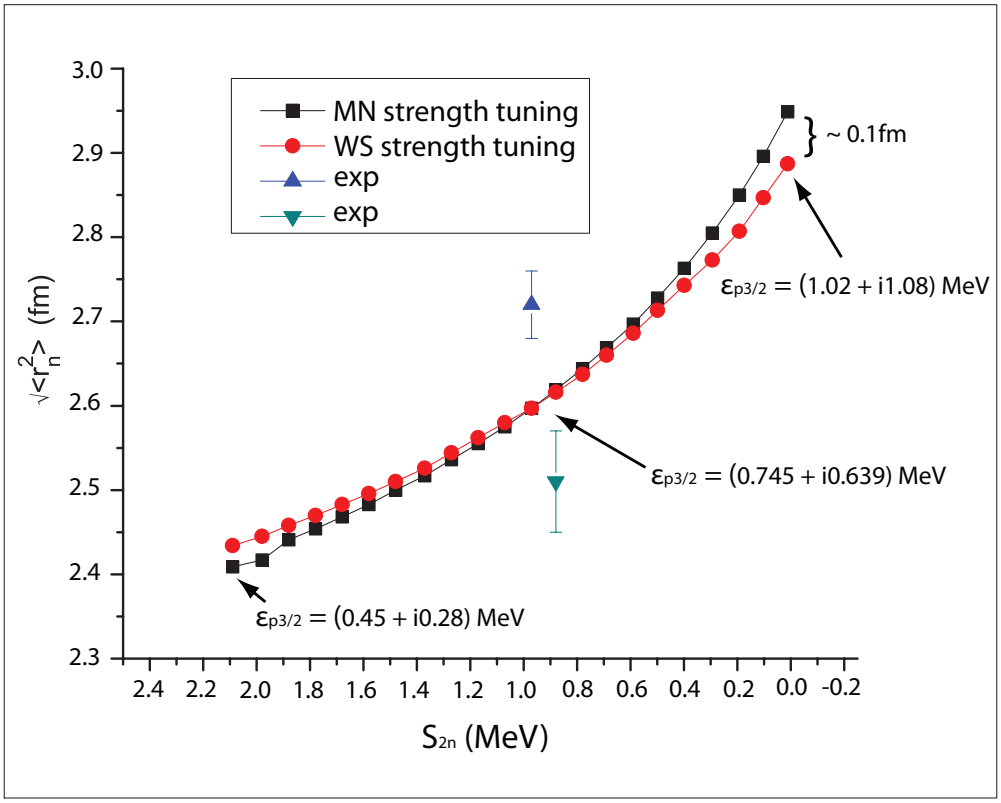


Figure 4.4: Similar to Fig.4.2 but for the rms neutron radius of ^{6}He. For the neutron rms the data were taken from [4].

correlations and also on the spatial properties of the system. In Fig.4.2 we plot the charge radius of the system as a function of the two-neutron separation energy. The red curve curve corresponds to the evolution of the charge radius when we keep the MMN interaction constant while changing the depth of the WS potential, namely the position of the $p_{3/2}$ resonance. We observe that the rate in which the charge radius is changing is different from the case where the $p_{3/2}$ resonance is fixed and the MMN interaction is modified (by altering the V_{os} strength) and more specifically in the limit of zero binding the charge radius that corresponds to a broad $p_{3/2}$ resonant

state is larger. The latter is indeed an indication of the impact of the position of the S-matrix pole (and thus of the continuum) on the pairing correlations, which in turn affects the radial properties of the system. We also calculate the rms neutron radius

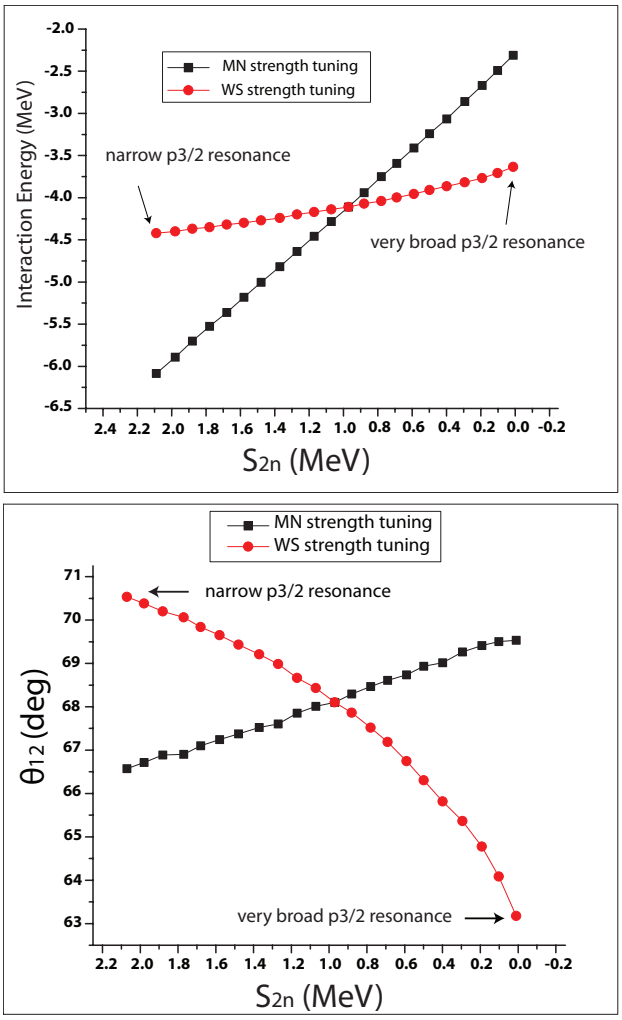


Figure 4.5: Dependence of the interaction energy, calculated as the expectation value of the two-body interaction (top panel) and correlation angle (bottom panel) of ^{6}He as a function of the two-neutron separation energy for the MMN force. The two different curves correspond to i) changing the MMN strength (black) and ii) changing the WS strength (red). See text for details.

to investigate the impact of the position of the resonant state on this observable. We find that the neutron rms radius is equal to $\sqrt{\langle r_n^2 \rangle} = 2.597$ fm. For the neutron radius of ^{4}He in (4.3) we used the assumption that $r^n_{rms}(^4\text{He}) = r^p_{rms}(^4\text{He}) = 1.527$

fm. In Fig.4.4 we observe that in the case of a broad $p_{3/2}$ resonance (Γ = (1.08

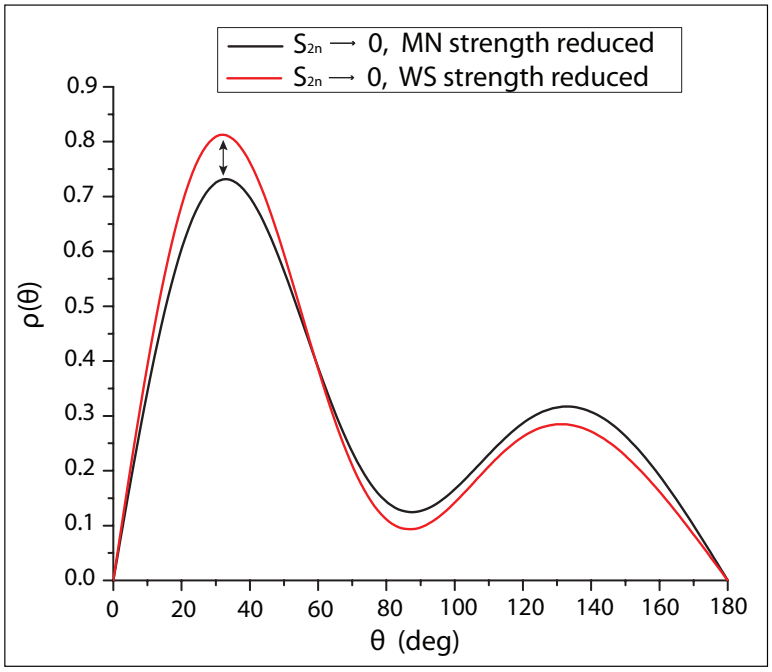


Figure 4.6: Angular densities of the ^{6}He g.s. It is shown the density when the S_{2n} = 0 MeV for the case of a very broad (shallow WS potential) $p_{3/2}$ resonance (red curve) and when S_{2n} = 0 MeV but for a weak two-body interaction.

MeV)) the neutron radius becomes smaller. This is indeed the PAH scenario. The neutron radius is more sensitive on the halo extent of the nucleus due to the additional $(r_1^2+r_2^2)$ diagonal term in (4.3). One observes in Fig.4.5 (top panel) that when the $p_{3/2}$ resonance becomes broader this results in an enhancement of the pairing correlations. This enhancement gives rise to a reduction of the radial extent of the system and hence a reduction of the neutron radius. On the other hand the charge radius was characterized by an increase.

The situation is slightly different for the charge radius. The charge radius-in the case of a broad $p_{3/2}$ resonance-is reduced (red line in Fig.4.2). The charge radius reflects both the halo extent and the correlations the valence neutrons (4.1). While the halo is reduced when the resonance becomes broader, the correlation of the particles is enhanced (angle is reduced, see formula (4.5)) as we see in Fig.4.5 (bottom panel). Overall, this combination leads in an increase of the charge radius.

The increased angular correlation in the vicinity of zero binding for the case of a broad $p_{3/2}$ resonance, is also reflected on the angular density in Fig.4.6 where the dineutron peak is enhanced while at the same time the cigarlike configuration is attenuated. Until now the PAH effect and the impact of the S-matrix poles positions on the radial properties of systems were investigated in a mean field theory framework. In our work we predict a similar phenomenon in a CI framework.

4.4.1 ^{8}He nucleus

Using Harmonic Oscillator states for high j partial waves

Before continuing to the results on ^{8}He, we shall test the possibility of using HO states in the basis, together with the Gamow states (mixed representation). Such mixed representation cannot be used in the SGI/SDI case. The results with these interactions exhibit a strong dependence on the maximal momentum used in the s.p basis. Because of that, results will depend on the s.p representation. In the MMN case the situation is different, since this interaction has practically no dependence on the k_{max} due to its full finite range. In the following test we will substitute the d-waves ($d_{5/2}$ and $d_{3/2}$) with HO states while the s-p states will be generated by the WS potential, with the $p_{3/2}$ as complex and the rest ($p_{1/2}$,$s_{1/2}$) taken as real non resonant continua. We will see that this combination of WS low angular momentum states and HO states for the ℓ >1 will result in smaller matrix dimensions, without altering the physics that governs a weakly bound system. The length of the HO was

Table 4.4: Impact of the HO states used to represent the d-waves on the g.s energy and point-proton radius of ^{6}He.

Observable	Full Calculation	Mixed Space
0^+ g.s energy	-0.975MeV	-0.974MeV
$\sqrt{\langle r^2_{pp}\rangle}$	1.846fm	1.843fm

taken to be b=2fm, and we consider ten HO shells for each d-wave: (i$d_{3/2}$ and i$d_{5/2}$) with $i \in (0, 9)$. The remaining basis components are the same as before: $0p_{3/2}$ is a

resonant state with 30 associated complex non-resonant continua along the contour, 21 $s_{1/2}$ real continua and 21 $p_{1/2}$ real continua up to k_{max}=4fm^{-1}. In Table 4.4 we compare values of the g.s energy and point-proton radius, for the full calculation (all basis states are Gamow states) and the mixed representation calculation (d-waves HO). The impact of the HO states on the radial density is illustrated in Fig.(4.7). As

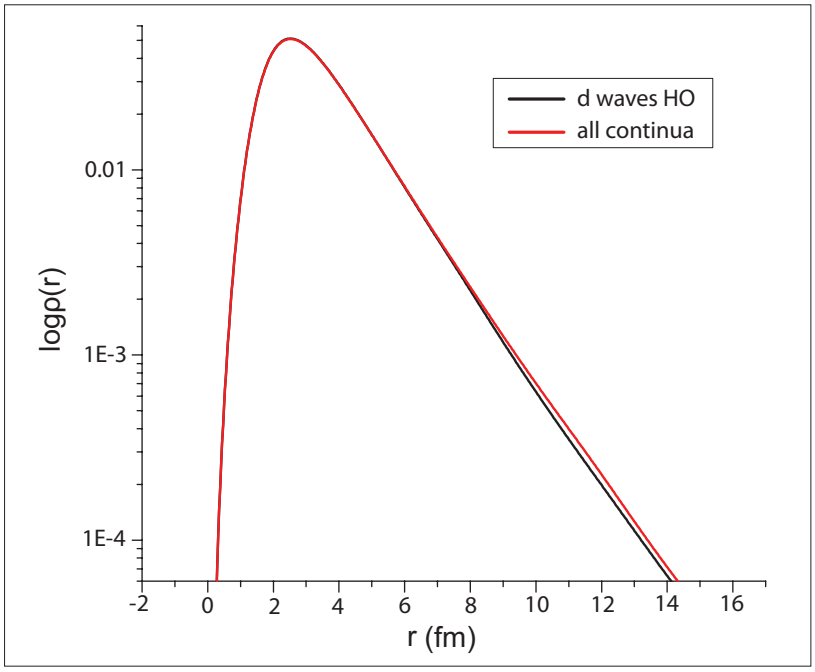


Figure 4.7: Radial density of the halo neutrons in ^{6}He in a full calculation (red) as compared to the calculation where the d-waves were represented by HO states.

we see in Table 3.2 the difference is of the order of 0.1keV in energy and 0.003fm in the proton radius. We see that the use of HO states for high angular momentum waves is equivalent to the full calculation. The total dimension for the full calculation is dim(M) = 12552, and for the mixed representation is dim(M) = 5303. This reduction may not seem to be very impressive for the light ^{6}He system, but for heavier systems or even in an ab-initio application of the GSM where partial waves up to $\ell = 8$ or larger should be used , this will clearly lead to more tractable calculations. In Fig.4.7 we present the density of the valence neutrons in a logarithmic scale. One can see that the radial properties of the system are very slightly affected.

4.4.2 GSM+DMRG application to the proton radius of ^{8}He

In this section we will present an application of the GSM+DMRG approach to calculate the charge radius of ^{8}He. With the current computing power, direct diagonalizations of the GSM Hamiltonian using either the Lanczos or the Davidson method, are possible for the lightest systems of the Helium, Lithium and Beryllium chains (^{6,7}He, ^{6,7}Li, ^{6,7}Be). For ^{8}He within a p-sd model space, one has to truncate the space of configurations to only two particles occupying the continuum orbits, in order to be able carry out full diagonalization. The dimensional catastrophe of the GSM is more severe compared to the Configuration Interaction Shell Model (CISM) in the HO basis. The matrix dimensions that one could handle in the GSM, are actually smaller than in typical CISM calculations, where dimensions of the 10^{11} order have already been reached in the pf shell [43]. The difference and the source of computational difficulties in the GSM, lies in the Hamiltonian matrix. In order to assure the completeness of the Berggren relation one should include, in general, a large amount of non-resonant scattering shells in the basis. The appearance of the non-resonant continuum states makes the matrix denser with much more non-zero matrix elements. As a consequence, the matrix times vector operation gets slower, and additionally more memory allocation is required. Even if there exist an adequate amount of memory, the calculation becomes very time consuming in model spaces with more than four partial waves and systems with more than four active particles. This limits the current GSM applications to matrix dimensions up to 10^6 in the m-scheme and it is the main reason for allowing only two particles occupying scattering states in the ^{8}He computation.

The basic goal of a truncation method aims at a reduction of the huge dimensionality of the CISM Hilbert space (or the Rigged Hilbert space of the GSM) while maintaining a high accuracy of the computed observables. We can truncate the space manually by allowing certain excitations (only one or two particles in the continuum) based on physical arguments (small weight of configurations with more

than two particles in the continuum). More sophisticated truncation methods allow the system itself to select the most important configurations, such us the Shell Model Monte Carlo [45], where the space is truncated stochastically. In the DMRG, the most important states are selected as the ones that correspond to the largest eigenvalues of the density matrix. This method is very successfully applied in the description of the properties of 1-d quantum lattices. Furthermore, the method has been used in Quantum Chemistry [118] and recently in nuclear structure [47, 48, 49, 29, 119, 50]. The generalization from quantum lattices to the study of finite Fermi systems is achieved by the replacement of lattice sites with s.p orbitals ($p_{3/2}$,$s_{1/2}$ etc). The procedure that follows is very similar and the only difference lies in the way the space of sites(s.p orbits) is defined and divided. For example, some authors divide the space between particles and holes [47] while others divide the space into proton and neutron states [48]. In our GSM context, we have noticed that the multiparticle non-resonant configurations contribution to the GSM wavefunction is relatively small. This calls for a division of the space into resonant states and non-resonant continuum states. In this way the most important configurations are taken into account (A-space) while the configurations from the B-space are gradually and systematically taken into account in each step. We may say that the GSM+DMRG is a very powerful method that provides a solution to the dimensionality problem by optimizing the number of non-resonant scattering states that will be used in the basis. It has been proven that this selection of important states in the GSM+DMRG, is determined by a complex variational principle [50], which is the complex analog of the usual variational principle for real matrices.

We shall proceed with the details of the calculation. In our application of the DMRG for the calculation of the ^{8}He charge radius, we are using the MMN force. The model space was the same as in the application of the Section 2.1, however this time we use less s.p states along the contours. In particular we discretized with 21 points each contour and we used ten HO states for the $d_{3/2}$ and $d_{5/2}$ waves, for a total of 84 s.p states. Even if we take 41 basis states less than in the previous calculations, the

g.s energy and the radius are almost unchanged. This means that the completeness has already been reached with 84 s.p states. The maximum GSM dimension in the m-scheme for this basis is dim(M) = 19,304,868. As we mentioned, due to the weak continuum-continuum coupling in the GSM wavefunction, the DMRG space is partitioned into a space A, containing resonant states and a space B containing the non-resonant continua. For a very detailed description of the DMRG process as it is used for the GSM, we refer to [50], however we will discuss some basic concepts and steps to make our discussion more clear.

The DMRG starts with the warm-up phase, which comprises a first approximation of the optimal wavefunction in the whole space. Initially all the many body basis states are constructed in the reference space A, say $|k_A\rangle$, and all the matrix elements of the second quantized Hamiltonian are calculated and stored:

$$a^\dagger, (a^\dagger \tilde{a})^K, (a^\dagger a^\dagger)^K, ((a^\dagger a^\dagger)^K \tilde{a})^L, (a^\dagger a^\dagger)^K (\tilde{a}\tilde{a})^K. \tag{4.10}$$

From this equation we also see that throughout the DMRG process the total angular momentum is conserved, as we work in a J-coupled scheme basis. The Hamiltonian is diagonalized on that basis to obtain the vector $|\Psi_J\rangle^0$, which we call the reference vector. Then the first shell from B is considered. All many body states relevant to this shell are constructed, say $|i_B\rangle$, and all the matrix elements of the Hamiltonian are calculated (4.10). Next, we obtain a basis by coupling the $|i_B\rangle$ states to $|k_A\rangle$ states and we diagonalize the Hamiltonian. Using a method that is also used in the GSM, the state of interest will be the one that maximizes the overlap with the reference vector. After this step, the density matrix is constructed and N_{opt} vectors are kept that correspond to its largest eigenvalues. In this optimized basis all the matrix elements of the suboperators in (4.10) are calculated and stored. The process continues until all scattering shells are exhausted and then the calculation takes place in the reverse order. This is the so-called sweep phase. In each step the system is growing systematically and the most important information is stored by calculating

the matrix elements of the operators. In DMRG the wavefunction is not stored. What is stored are the matrix elements of the second quantization operators of dimension N_{opt}. These operators define not only the Hamiltonian but any other operator in the Fock space. Hence, we are able to calculate in each step expectation values of all observables of interest, such us the charge radius. In order to complete the calculation

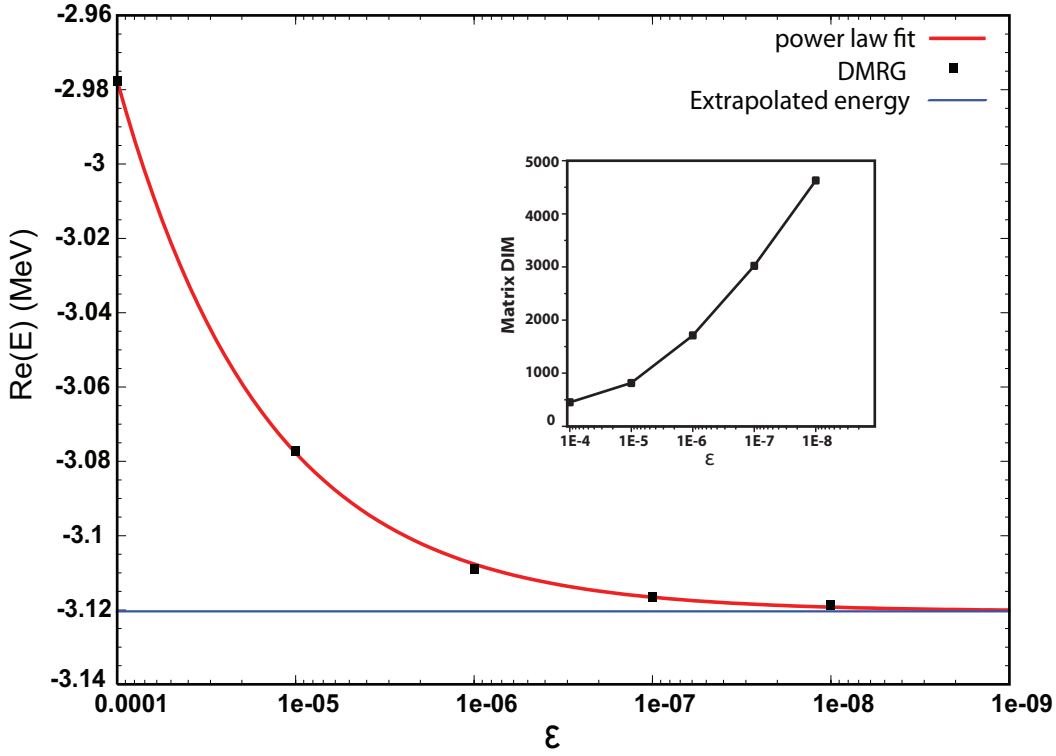


Figure 4.8: Convergence pattern of the real part of the energy in ^{8}He as a function of the ϵ. In the inset shows the dimension of the DMRG matrix versus ϵ.

of the observable, we need to compute, one and two-body matrix elements of an operator. In the case of the charge radius these are given by (4.2). These integrals are calculated in the Gamow basis and they are the input for the calculation of the expectation value of the radius operator.

Our experience [50] has shown that it is important to consider in the reference space A, not only resonant states but also some non-resonant scattering shells from the B space, in order to generate all possible many-body configurations in the warm-up phase. So in addition to the $0p_{3/2}$ resonant state, the space A contained also the

last $s_{1/2}$ non-resonant scattering state and the last $d_{5/2}$, $d_{3/2}$ HO states respectively. The choice of the shell to be included in the pole space A is arbitrary and the results do not depend on which shell is considered. The mixture of positive and negative parity states assures that we will not miss any couplings in the warm-up phase. In the space B the shells are ordered like: $\{ip_{3/2}, ip_{1/2}, id_{5/2}, id_{3/2}\}$ where i denotes the scattering shell starting from 0. In the case of the d-states $i \in (0, 9)$ denotes the HO radial quantum number. Usually, in DMRG applications, it is decided from

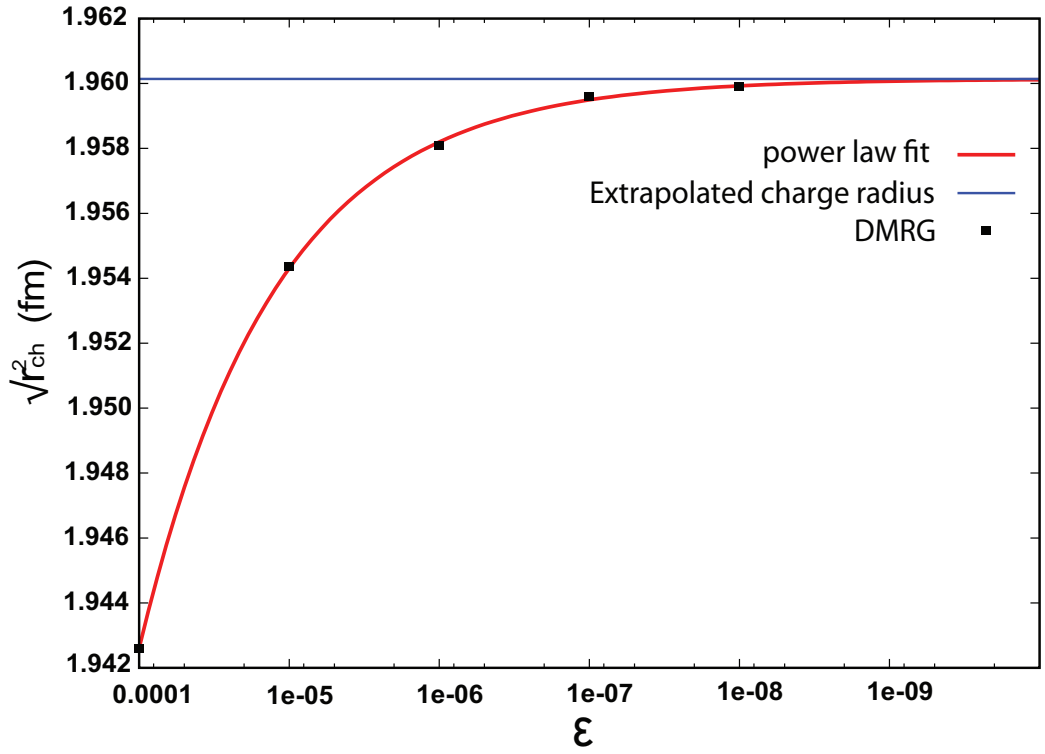


Figure 4.9: Convergence pattern of the charge radius in ^{8}He as a function of the ϵ.

the beginning how many states of the density matrix, corresponding to the largest eigenvalues, are kept. This number is then fixed throughout the whole process. In this work we will use a truncation scheme that has been used very recently in the GSM+DMRG framework [50] and has been proposed in [120]. It suggests that N_ρ

vectors satisfy the inequality:

$$\left| 1 - Re\left(\sum_{\alpha=1}^{N_\rho} w_\alpha \right) \right| < \epsilon \tag{4.11}$$

are kept in each step. The smaller the ϵ the more vectors are kept. This method is called dynamical block selection approach and owes its name to the fact that N_ρ changes during the process.

Table 4.5: Impact of the model space truncation on the energy and charge radius.

Truncation	^{8}He g.s energy	^{8}He rms radius
2p-2h	-2.98	1.964
4p-4h	-3.11	1.961

Using the parameters that were fitted to the ^{6,8}He g.s energies and performing a GSM calculation but only allowing two particles occupying continuum orbits (2p-2h), we find that the system is underbound by $\sim$ 100keV (Table.4.5). This is something that we expect, since now the calculation does not uses the whole space and reveals the variational nature of the DMRG. It is also seen that diagonalizing the Hamiltonian in the GHF basis, the weight of configurations with more than two particles in the continuum is small, hence the gain in energy is also small. For the full GSM+DMRG calculations the truncation error is ϵ=10^{-8} resulting in a maximum number of vectors kept N_ρ=123 and a maximum dimension of a matrix to be diagonalized with dim=4622. The calculations that we present in Table 4.7 correspond to the end of the second sweep. We observe that for decreasing values of ϵ the DMRG dimensions are increased. Additionally, the changes in energy and the radius are decreased rapidly. In Fig.(4.8) and Fig.(4.9) we see that both the energy and the radius are characterized by a power law convergence pattern. The function that the points were fitted is the following:

$$y(\epsilon) = a + b\epsilon^c \tag{4.12}$$

Table 4.6: Energy and charge radius of ^{8}He for different truncation errors of the density matrix. The last column presents the maximum dimension of matrix to be diagonalized each time. See also Fig.(4.8) inset.

ϵ	Energy (MeV)	$\sqrt{r^2_{ch}}$ (fm)	$\dim_{max}$
10^{-4}	-2.9787	1.9437	452
10^{-5}	-3.07719	1.95545	815
10^{-6}	-3.10893	1.95919	1712
10^{-7}	-3.11653	1.96069	3022
10^{-8}	-3.11872	1.9609	4622

which was also used in the very recent application of the DMRG to the two fluid open quantum systems. The extrapolated values in this case are: $E^{\epsilon\to 0}_{extp}$=-3.12029MeV and $\sqrt{r^2_{ch}}^{\epsilon\to 0}_{extp}$=1.961fm. This power law convergence could be very useful in larger systems (^{11}Li, ^{11}Be), where a calculation for large ϵ (small space) would be enough in order to estimate the energy or any other observable by extrapolation. For the neutron rms radius we obtain that $\sqrt{r^2_{n}}^{\epsilon\to 0}_{extp}$=2.77fm. We would like to mention that there is no reference about the imaginary parts of the energy and the radius because they were negligible. The $Im[E]$ is of the order of 0.1keV and the $Im[r_{ch}]$ is of the order of 10^{-4}fm, which means that the Berggren completeness is fulfilled numerically.

^{8}He results and comparisons with other models and experiment.

In this Section we discuss the results of our calculations for the charge and neutron radii in ^{8}He. In the results for charge radius we have already taken into account the finite size effects, the core polarization (6.66% for ^{8}He) and the s.o correction. For the latter we found that:

$$\langle r^2\rangle_{so} = \int r^2 \rho_{so}(r)\, dr = -0.158 fm^2.$$

We see that it is almost double in absolute value as compared to the s.o correction of ^{6}He (-0.0718fm^{-2}). In Table.4.7 we show the results for the ^{6,8}He rms radii in the GSM as compared with other theories and the experiment. The matter radius

is calculated from the relation $r_m^2 = \frac{1}{A}(Zr_p^2 + Nr_n^2)$. Our calculations reproduce the experimental trend which indicates the decrease in the charge radius from ^{6}He to ^{8}He. This decrease is explained by the fact that the valence neutrons spend less

Table 4.7: Comparison of the GSM rms charge radius with other theories and experiment. The values of the s.o contribution are also presented. Experimental values for the neutron and matter rms radii are taken from [2, 3, 4, 5, 6, 7, 8, 9].

	$\sqrt{\langle r_{ch}^2\rangle}$[fm]				
	GSM	NCSM	GFMC	Exp	$\langle r_{so}^2\rangle$[fm^2] †
^{6}He	2.026	2.009	2.037	2.068(11)-2.054(14)	-0.072 (-0.08)
^{8}He	1.961	1.972	1.91	1.929(26)	-0.158 (-0.17)

	$\sqrt{\langle r_n^2\rangle}$[fm]			
	GSM	NCSM	GFMC	Exp
^{6}He	2.597	2.67	2.82	2.46-2.85
^{8}He	2.77	2.80	2.96	2.67-2.81

	$\sqrt{\langle r_m^2\rangle}$[fm]			
	GSM	NCSM	GFMC	Exp
^{6}He	2.38	2.43	2.55	2.30-2.71
^{8}He	2.58	2.6	2.73	2.42-2.52

time as a correlated pair in ^{8}He. We found that the probability of a di-neutron configuration is $\sim 60\%$ while for a cigar-like is $\sim 40\%$ (see Fig.3.7). We noticed that the positions of the maxima of the angular densities are not changed in ^{6,8}He but only the relative weights change. On average the di-neutron in ^{8}He is found with angle $\theta_{nn} = 78^o$ while in ^{6}He the di-neutron angle was $\theta_{nn} = 68^o$. By simple geometrical considerations, we can deduce the average distance of the two nucleons from the core in ^{6,8}He. This is calculated by the relation $r_{c-2n} = \cos(\frac{\theta_{nn}}{2})|r_1|$. We find that $r_{c-2n} =$ 2.96fm (3.36fm exp) for ^{6}He and $r_{c-2n} = 2.58$fm for ^{8}He. The experimental value for the core-dineutron distance exist only for ^{6}He [121] and our results are consistent with this value. Overall the recoil is smaller in ^{8}He. This behavior is depicted in Fig.4.10 where the effects of s.o, core-polarization and finite size corrections are included. Additionally, the s.o contribution calculated with our model has a non negligible effect on the rms charge radius of ^{6,8}He. Its value is comparable to the finite size effects of the proton and neutron and it is responsible for a further decrease of the

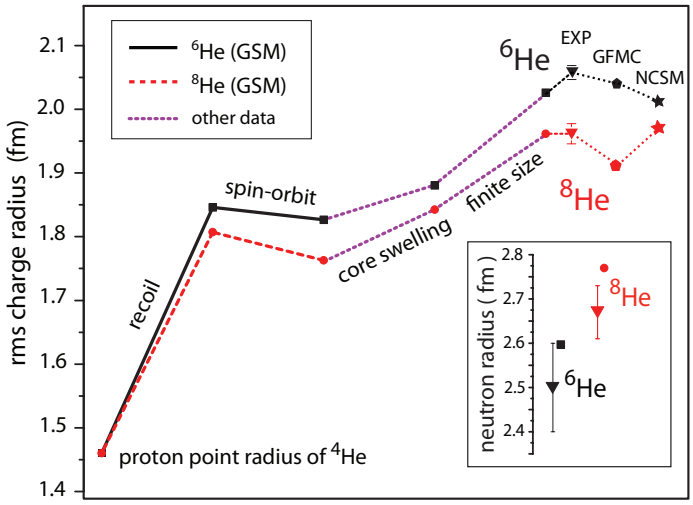


Figure 4.10: Different contributions to the charge radius of ^{6}He (solid line, squares) and ^{8}He (dashed line, dots) calculated in GSM. The core swelling contribution is taken from GFMC calculations of Ref. [10]. Recently revised experimental charge radii come from [11] (triangles). The NCSM [12] (stars) and GFMC [13] (pentagons) results are marked for comparison. The inset shows GSM rms neutron radii compared to experiment [8].

charge radius of ^{8}He. The point-proton radius of ^{8}He was calculated to be slightly smaller than the one of ^{6}He and when we convert the point radius to charge radius, by also including the s.o correction, the decrease is enhanced making a better contact with the experiment. Hence, the ^{8}He charge radius decrease is not only a geometrical phenomenon but it is also caused by the large s.o correction in ^{8}He. As it was argued in [122] that the D.F term should be explicitly considered as a part of the charge density operator. Considering that the s.o term arises from the same transformation of the 4-component relativistic wavefunction into the non-relativistic form, there is no specific reason to neglect this term from the analysis of charge radii. By inspecting the formula (2.19) we see that the s.o rms radius is a model-dependent quantity. However, when we compare our results with the last column of Table 4.7 which is a maximal s.p. estimate, we do not notice big deviations. We thus conclude that the s.o term is an important quantity for the detailed description of the charge distribution in halo nuclei, but is weakly affected by the correlations. While the core-polarization

tends to increase the charge radius, the combination of all the effects results in a total decrease of the charge radius in ^{8}He.

4.5 Concusions and Future Plans

In this work we performed calculations for the charge radii of the neutron halo nuclei, ^{6}He and ^{8}He, in the framework of the GSM. The GSM is a model that assures the correct asymptotic behavior of the wavefunctions and the correct description of systems lying in the neutron rich side of the nuclear chart. The adoption of COSM coordinates that result in a Hamiltonian that is free of spurious center-of-mass motion, is a decisive step for the realistic description of a phenomenon that could be only explained by the relative motion of the subsystems of the halo system. Our main objective was to examine the phenomenology and understand the physics behind the charge radii changes of halos, rather than to construct the effective nuclear interaction. For that reason we limited ourselves to a small number of interaction parameters. The findings of this work however could be used in constraining more advanced GSM Hamiltonians.

One of the basic conclusions was that the detailed description of the ^{6}He charge radius requires the precise knowledge of S_{2n}. We noticed that when this condition is met the $p_{3/2}$ occupation comprises almost a 90% of the total wavefunction. For this percentage the radial extent of the halo and the geometry of the neutrons is such, so as the rms charge radius is close to the experiment. Our calculations reproduced the experimental trend of the charge radius of ^{6}He being larger than that of the α-core and that of ^{8}He being smaller than that of ^{6}He. For ^{6}He we demostrated, by calculating the correlation density, that indeed the valence neutrons are correlated in a manner that increases the orbital motion of the core around the CoM and hence the charge radius. We confirmed that the g.s wavefunction is dominated by an S = 0 component which extends to large distances away from the core and the neutrons in this state are well correlated (di-neutron), giving rise to an enhanced recoil motion

and thus an increased charge distribution. This dineutron configuration in ^{6,8}He is strongly enhanced by coupling to the nonresonant continuum. We also predicted that the neutrons in the 2^+ state of ^{6}He are almost uncorrelated with an average opening angle of $\sim 83^o$.

We applied the GSM+DMRG approach in the calculation of the ^{8}He charge radius, and this has led to highly accurate results. This should open up a window in extending our studies of weakly bound nuclei to larger configuration spaces. We demonstrated that the reduction of the charge radius when going from ^{6}He to ^{8}He is not due to a more "democratic" arrangement of the neutrons around the core but rather due to the reduction of the amplitude of the dineutron configuration in the g.s. wave function, resulting in a smaller core recoil radius. In addition, the negative s.o. radius contribution doubles with the addition of two valence neutrons. Apart from this geometrical effect, the calculated s.o contribution leads to a further decrease of the ^{8}He charge radius. It turns out that this quantity can be comparable to the DF term and it should not be neglected in a detailed analysis. The charge distribution in Helium halos is consistently described by the orbital motion of the core around the common nuclear CoM, the polarization of the core by the valence neutrons and the s.o contribution caused by the anomalous magnetic moment of the neutron. We have also studied the dependence of the two-body interaction and the radii on the position of the S-matrix poles. This was shown by the different rate of change of the rms charge and neutron radius with S_{2n} of ^{6}He when i) modifying the WS depth or ii) altering the strength of the force. This is a one aspect of the PAH effect which was considered for first time in a configuration interaction framework.

Using relatively simple forces and a small amount of parameters, we achieved calculations comparable in quality with the state of the art ab-initio calculations which use high precision realistic interactions. Based on our charge radius studies, we conclude that the recent experiments on charge radii of halo nuclei put a stringent constraint on the GSM Hamiltonian and they can be used as benchmarks for testing the models that are proposed for the nuclear interaction.

In a future work we will enrich the form of our effective interaction with the addition of spin-orbit tensor terms. The addition of these parts in the Hamiltonian is crucial for a realistic description the nucleus. The two-body spin-orbit potential for example will cause (through the HF procedure) the microscopic one-body spin-orbit term in the average single particle nuclear potential, which is an important ingredient for the shell structure. This force actually has the same mathematical form with the AV8$'$ [40] and the difference lies only on the form factors. The AV8$'$ is fitted in order to reproduce the NN scattering phase shifts, however we can find in the bibliography parameterizations of this force onto nuclear properties [123, 124]. In our case the parameters will be determined by fitting several nuclei in the p-sd model space. Contrary to the CISM in a HO basis, where all the matrix elements in a given model space are adjusted to experimental data, the process of constructing the effective interaction in GSM, resembles the Skyrme and the Gogny phenomenology of the mean field approach. We start from a general form of a force, that is consistent with the symmetries of the nuclear Hamiltonian and we determine the parameters by fitting it on g.s or excited state properties of several nuclei. Such an interaction is urgently needed for the detailed description of weakly bound systems within the OQS framework of GSM. One of the future directions is to construct an ab-initio Gamow Shell Model theory. The NCSM [37] has had a lot of success in describing the structure of light nuclei using high precision realistic forces. However the HO basis that the NCSM machinery employs might not be very suitable for the description of the large radial extent of halo nuclei, the coupling to the continuum etc. A complementary approach would be to combine the NCSM approach with the GSM to study in an ab-inito manner nuclei far from stability.

Bibliography

Bibliography

[1] D. R. Tilley *et al.* *Nucl.Phys.A*, 745:155, 2004. vii, 26

[2] I. Tanihata *et al.* *Phys.Rev.Lett*, 55:2676, 1985. viii, 59

[3] I. Tanihata *et al.* *Phys.Lett.B*, 206:592, 1988. viii, 59

[4] I. Tanihata *et al.* *Phys.Lett.B*, 289:261, 1992. viii, xi, 47, 59

[5] A. Ozawa, T. Suzuki, and I. Tanihata. *Nucl.Phys.A*, 693:32, 2001. viii, 59

[6] I. Tanihata *et al.* *Phys.Lett.B*, 160:380, 1985. viii, 59

[7] J. S. Al-Khalili, J. A. Tostevin, and I. J. Thompson. *Phys.Rev.C*, 54:1843, 1996. viii, 59

[8] G. D. Alkhazov *et al.* *Phys.Rev.Lett*, 78:2313, 1997. viii, xii, 21, 59, 60

[9] I. B. Shostak *et al.* *Phys.Rev.C*, 63:017602, 2000. viii, 59

[10] S. C. Pieper. *Riv. Nuovo Cim.*, 031:709, 2008. xii, 45, 60

[11] M. Brodeur *et al.* arXiv:1107.1684, 2011. xii, 3, 22, 60

[12] E. Caurier and P. Navrátil. *Phys.Rev.C*, 73:021302, 2006. xii, 60

[13] S. C. Pieper and R. B. Wiringa. *Annu.Rev.Part.Sci*, 51:53, 2001. xii, 4, 5, 24, 60

[14] Rare Isotope Science Assessment Committee NAS/NRC. *Scientific Opportunities with a Rare-Isotope Facility in the United States*. The National Academies Press, 2007. 1

[15] H.-P. Breuer and F. Petruccione. *The Theory of Open Quantum Systems*. Oxford University Press, Oxford, 2002. 2

[16] E.B. Davies. *Quantum Theory of Open Systems*. Academic Press, London, 1976. 2

[17] A.I. Magunov, I. Rotter, and S.I. Strakhova. *J.Phys.B.*, 32:1669, 1999. 2

[18] Y. Alhassid. *Rev.Mod.Phys.*, 72:895, 2000. 2

[19] S. Inouye *et al. Nature*, 392:151, 1998. 2

[20] N. Michel, W. Nazarewicz, J. Okołowicz, and M. Płoszajczak. *J.Phys.G: Nuclear and Particle Physics*, 37:064042, 2010. 2, 7

[21] J. Dobaczewski, N. Michel, W. Nazarewicz, M. Płoszajczak, and J. Rotureau. *Prog.Part.Nucl.Phys.*, 59:432, 2007. 2, 46

[22] J. Okołowicz, M. Płoszajczak, and I. Rotter. *Phys.Rep*, 374:271, 2003. 2

[23] I. M. Gel'fand and N. Ya. Vilenkin. *Generalized Functions, Vol4*. Academic Press, New York, 1961. 2

[24] K. Maurin. *Generalized Eignefunction Expansions and Unitary Representation of topological Groups*. Polish Scientific Publishers, Warsaw, 1968. 2

[25] A. Bohm. *The Rigged Hilbert Space and Quantum Mechanics*. Lecture Notes in Physics 78, Springer, New York, 1978. 2

[26] K.M. Nollett *et al. Phys.Rev.Lett*, 99:022502, 2007. 2, 6

[27] S. Quaglioni and P. Navratil. *Phys.Rev.Lett*, 101:092501, 2008. 2, 6

[28] G. Hagen, T. Papenbrock, and M. Hjorth-Jensen. *Phys. Rev. Lett*, 104:182501, 2010. 2

[29] J. Rotureau, N. Michel, W. Nazarewicz, M. Płoszajczak, and J. Dukelsky. *Phys.Rev.Lett*, 97:110603, 2006. 2, 6, 53

[30] L.B. Wang *et al.* *Phys.Rev.Lett*, 93:142501, 2004. 3, 22

[31] P. Mueller *et al.* *Phys.Rev.Lett*, 99:252501, 2008. 3, 22

[32] P.F. Bedaque and U. van Kolck. *Ann. Rev. Nucl. Part. Sci.*, 52:339, 2002. 3

[33] E. Epelbaum, H. W. Hammer, and U. G. Meissner. *Rev. Mod. Phys.*, 81:1773, 2009. 3

[34] E. Epelbaum. *Prog. Part. Nucl. Phys.*, 57:654, 2006. 3

[35] D. R. Entem and R. Machleidt. *Phys. Rev. C*, 68:041001, 2003. 3, 5

[36] E. Epelbaum, W. Glockle, and U. G. Meissner. *Nucl. Phys. A*, 747:362, 2005. 3, 5

[37] P. Navratil, S. Quaglioni, I. Stetcu, and B. R. Barrett. *J. Phys. G: Nucl. Part. Phys.*, 36:083101, 2009. 4, 63

[38] S. C. Pieper, R. B. Wiringa, and J. Carlson. *Phys. Rev. C*, 70:054325, 2004. 4

[39] G. Hagen, T. Papenbrock, D. J. Dean, and M. Hjorth-Jensen. *Phys. Rev. C*, 82:034330, 2010. 4

[40] R. B. Wiringa, V. G. J. Stoks, and R. Schiavilla. *Phys.Rev.C*, 51:38, 1995. 5, 63

[41] Machleidt. R. *Phys. Rev. C*, 63:024001, 2001. 5

[42] S. K. Bogner, R. J. Furnstahl, and A. Schwenk. *Prog. Part. Nucl. Phys.*, 65:147, 2010. 5

[43] E. Caurier, F. Martínez-Pinedo, Nowacki, A. Poves, and A. Zuker. *Rev.Mod.Phys.*, 77:427, 2005. 5, 52

[44] D. J. Dean, T. Engeland, M. Hjorth-Jensen, M. P. Kartamyshev, and E. Osnes. *Prog. Part. Nucl. Phys.*, 53:419, 2004. 5

[45] S.E. Koonin, D.J. Dean, and K. Langanke. *Phys. Rep.*, 278:1, 1997. 6, 53

[46] C. W. Johnson, S. E. Koonin, G. H. Lang, and W. E. Ormand. *Phys. Rev. Lett*, 69:1992, 1992. 6

[47] J. Dukelsky, S. Pittel, and M. Dimitrova, S.and Stoitsov. *Phys.Rev.C*, 65:054319, 2002. 6, 53

[48] T. Papenbrock and D. J. Dean. *J.Phys.G*, 31:S1377, 2005. 6, 53

[49] S. Pittel and N. Sandulescu. *Phys.Rev.C*, 73:014301, 2006. 6, 53

[50] J. Rotureau, N. Michel, W. Nazarewicz, M. Płoszajczak, and J. Dukelsky. *Phys.Rev.C*, 79:014304, 2009. 6, 53, 54, 55, 56

[51] M. Bender, P.-H. Heenen, and P.-G. Reinhard. *Rev. Mod. Phys.*, 75:121, 2003. 6

[52] M. Kortelainen, T. Lesinski, J. Moré, W. Nazarewicz, J. Sarich, N. Schunck, M. V. Stoitsov, and S. Wild. *Phys. Rev. C*, 82:024313, 2010. 6

[53] N. Schunck, J. Dobaczewski, J. Moré, J. McDonnell, W. Nazarewicz, J. Sarich, and M. V. Stoitsov. *Phys. Rev. C*, 81:024316, 2010. 6

[54] G. Hagen *et al. Phys.Lett.B*, 656:169, 2007. 6

[55] A. Volya and V. Zelevinsky. *Phys.Rev.C*, 74:064314, 2006. 6

[56] K. Bennaceur, F. Nowacki, J. Okołowicz, and M. Płoszajczak. *Nucl. Phys. A*, 651:289, 1999. 6

[57] N. Michel, W. Nazarewicz, M. Płoszajczak, and T. Vertse. *J.Phys.G:Nucl.Part.Phys*, 36:013101, 2009. 6, 13

[58] K. Ikeda, T. Myo, K. Kato, and T. Hiroshi. *Lecture Note in Physics*, 818, 2010. 7, 44

[59] J. Dobaczewski, H. Flocard, and J. Treiner. *Nucl. Phys. A*, 422:103, 1984. 7

[60] J. Dobaczewski, W. Nazarewicz, T. R. Werner, C.R. Berger, C.R. Chinn, and J. Dechargé. *Phys. Rev. C*, 53:2809, 1996. 7, 8

[61] N. Michel, K. Matsuyanagi, and M. Stoitsov. *Phys. Rev. C*, 78:044319, 2008. 7

[62] J.B. Ehrman. *Phys. Rev.*, 81:412, 1951. 7

[63] R.G. Thomas. *Phys. Rev.*, 88:1109, 1952. 7

[64] N. Michel, W. Nazarewicz, and M. Płoszajczak. *Phys.Rev.C*, 82:044315, 2010. 8, 13

[65] B.P. Wigner. *Phys. Rev.*, 73:1002, 1948. 8

[66] N. Michel, W. Nazarewicz, and M. Płoszajczak. *Phys.Rev.C*, 75:031301, 2007. 8

[67] N. Michel, W. Nazarewicz, and M. Płoszajczak. *Nucl. Phys. A*, 794:29, 2007. 8

[68] M. Beiner, R. J. Lombard, and D. Mas. *Nucl. Phys. A*, 249:1, 1975. 8

[69] T. Berggren. *Nucl.Phys.A*, 109:265, 1968. 11

[70] T. Berggren and P. Lind. *Phys.Rev.C*, 47:2, 1993. 12

[71] B. Gyarmati and T. Vertse. *Nucl.Phys.A*, 160:523, 1971. 12

[72] N. Michel, W. Nazarewicz, M. Płoszajczak, and K. Bennaceur. *Phys.Rev.Lett*, 89:042502, 2002. 13, 16, 17

[73] N. Michel, W. Nazarewicz, M. Płoszajczak, and J. Okołowicz. *Phys.Rev.C*, 67:054311, 2003. 13, 16

[74] N. Michel, W. Nazarewicz, and M. Płoszajczak. *Phys.Rev.C*, 70:064313, 2004. 13, 17, 18

[75] D. H. Gloekner and R. D. Lawson. *Phys.Lett.B*, 53:4, 1974. 13

[76] M. V. Zhukov *et al.* *Phys.Rep.*, 231:151, 1993. 13, 27

[77] Y. Suzuki and K. Ikeda. *Phys.Rev.C*, 38:1, 1988. 13, 40

[78] G. Hagen, M. Hjorth-Jensen, and N. Michel. *Phys.Rev.C*, 73:064307, 2006. 13

[79] A.T. Kruppa, G. Papadimitriou, N. Michel, and W. Nazarewicz. In Preparation, 2011. 14, 29

[80] N. Michel. *Eur.Phys.J.A*, 73:523–527, 2009. 16

[81] S. Saito. *Prog.Theor.Phys.*, 41:705, 1969. 16

[82] I. C. Green and S. A. Moszkowski. *Phys.Rev*, 139:B790, 1965. 17

[83] D. R. Thompson, M. LeMere, and Y. C. Tang. *Nucl.Phys.A*, 268:53, 1977. 17, 18, 19

[84] I. Sick. *Phys.Lett.B*, 116:212, 1982. 21, 24

[85] *et al* A. Amroun. *Nucl. Phys. A*, 579:596, 1994. 21

[86] R. Sánchez *et al.* *Phys.Rev.Lett*, 96:033002, 2006. 22

[87] W. Nörtershäuser *et al.* *Phys.Rev.Lett*, 102:062503, 2009. 22

[88] J. L. Friar and J. W. Negele. *Adv.Nucl.Phys*, 8:219, 1975. 23

[89] W. Bertozzi, J. L. Friar, J. Heisenberg, and J. W. Negele. *Phys.Lett.B*, 41:408, 1972. 23

[90] A. Ong, J.C. Berengut, and V.V. Flambaum. *Phys.Rev.C*, 82:014320, 2010. 23

[91] R. B. Wiringa. private communication, 2008. 24

[92] R. B. Wiringa and S. C. Pieper. private communication, 2011. 24

[93] V.I. Kukulin, V.M. Krasnopolsky, V.T. Voronchev, and P.B. Sazonov. *Nucl.Phys.A*, 453:365, 1986. 27

[94] V.I. Kukulin, V.N. Pomeranchev, Kh.D. Ratikov, V.T. Voronchev, and G.G. Ryzhikh. *Nucl.Phys.A*, 586:151, 1995. 27, 36

[95] G. F. Bertsch and H. Esbensen. *Ann.Phys.(N.Y.)*, 209:327, 1991. 27

[96] E. Nielsen, D.V Fedorov, A.S. Jensen, and E. Garrido. *Phys.Rep.*, 347:373, 2001. 27

[97] K. Hagino and H. Sagawa. *Phys.Rev.C*, 72:044321, 2005. 27, 45

[98] Y. Kikuchi, K. Kato, T. Myo, M. Takashina, and K. Ikeda. *Phys.Rev.C*, 81:044308, 2010. 27

[99] I. Brida and F.M. Nunes. *Nucl.Phys.A*, 847:1, 2010. 27

[100] Yu. Ts. Oganessian, V. I. Zagrebaev, and J. S. Vaagen. *Phys.Rev.Lett*, 82:4996, 1999. 27, 30

[101] F. M. Marqués *et al.* *Phys.Rev.C*, 64:061301, 2001. 28

[102] Nigel Orr. RCNP, Spring Workshop on Cluster Condensation and Nucleon Correlations, 2008. 28

[103] A.M. Frolov and V.H. Smith. *Phys.Rev.A*, 53:3853, 1996. 29

[104] M. V. Zhukov *et al.* *Phys.Rev.C*, 43:2835, 1991. 31

[105] C. A. Bertulani and M. S. Hussein. *Phys.Rev.C*, 76:051602, 2007. 42

[106] K. Hagino and H. Sagawa. *Phys.Rev.C*, 76:047302, 2007. 42

[107] T. Suzuki and T. Otsuka. *Phys.Rev.C*, 56:847, 1997. 44

[108] G. F. Bertsch, K. Hencken, and H. Esbensen. *Phys.Rev.C*, 57:1366, 1998. 44

[109] H. Simon *et al.* *Phys.Rev.Lett*, 83:496, 1999. 44

[110] S. Cohen and D. Kurath. *Nucl.Phys.*, 73:1, 1965. 45

[111] K. Bennaceur, J. Dobaczewski, and M. Płoszajczak. *Phys.Rev.C*, 60:034308, 2000. 46

[112] K. Hagino and H. Sagawa. *Phys.Rev.C*, 84:011303, 2011. 46

[113] M. Yamagami. *Eur. Phys. J. A.*, 25:569, 2005. 46

[114] M. Yamagami. *Phys. Rev. C*, 72:064308, 2005. 46

[115] V. Rotival and T. Duguet. *Phys. Rev. C*, 79:054308, 2009. 46

[116] V. Rotival, T. Duguet, and K. Bennaceur. *Phys. Rev. C*, 79:054309, 2009. 46

[117] K. Riisager, A.S. Jensen, and P. Møller, 1992. 46

[118] G. K-L. Chan and M. Head-Gordon. *J.Chem.Phys*, 116:4462, 2002. 53

[119] B. Thakur, S. Pittel, and N. Sandulescu. *Phys.Rev.C*, 78:041303, 2008. 53

[120] Ö. Legeza, J. Röder, and B. A. Hess. *Phys.Rev.B*, 67:125114, 2003. 56

[121] T. Aumann *et al.* *Phys.Rev.C*, 59:1252, 1999. 59

[122] J.L. Friar, J. Martorell, and D.W.L. Sprung. *Phys.Rev.A*, 56:4579, 1997. 60

[123] H. Furutani, H. Horiuchi, and R. Tamagaki. *Prog.Theor.Phys.*, 62:981, 1979. 63

[124] D. Gogny, P. Pires, and R. De Tourreil. *Phys.Lett*, 32B:591, 1970. 63

[125] H. Kanada, T. Kaneko, N. Shinobu, and N. Morikazu. *Prog. Theor. Phys.*, 61:1327, 1978. 81

Appendix

Appendix A

Two body density and correlation density

We present the formulas and the definitions of the two-body density and correlation density. The formal definition of the two-body density is given as:

$$\rho(\boldsymbol{r}, \boldsymbol{r'}) = \langle \Psi | \delta(\boldsymbol{r} - \boldsymbol{r}_1) \delta(\boldsymbol{r'} - \boldsymbol{r}_2) | \Psi \rangle \tag{A.1}$$

where $|\Psi\rangle$ is a quantum mechanical state of the nucleus (g.s or excited state). Using the expression of the δ function in spherical coordinates

$$\delta(\boldsymbol{r} - \boldsymbol{r}_1) = \frac{1}{r^2 \sin(\theta)} \delta(r - r_1) \delta(\theta - \theta_{12}) \delta(\phi - \phi_{12}) \tag{A.2}$$

and consider azimuthal symmetry (the ϕ integral is projected out), we have:

$$\delta(\boldsymbol{r} - \boldsymbol{r}_1) = \frac{1}{2\pi r^2 \sin(\theta)} \delta(r - r_1) \delta(\theta - \theta_{12}) \tag{A.3}$$

For the second radial δ we obtain:

$$\delta(\boldsymbol{r'} - \boldsymbol{r}_2) = \frac{1}{4\pi r'^2} \delta(r' - r_2) \tag{A.4}$$

Inserting A.3 and A.4 to A.1 we obtain that:

$$\langle\Psi|\delta(r-r_1)\delta(r'-r_2)\delta(\theta-\theta_{12})|\Psi\rangle = 8\pi^2 r^2 r'^2 \sin(\theta)\rho(\boldsymbol{r},\boldsymbol{r'}) \tag{A.5}$$

This is the connection between the two-body density and the correlation density that calculated in Chapter 3 The two-body density has dimensions of $[fm^{-6}]$ while the correlation density is in $[fm^{-2}]$.

A.1 Matrix Elements of the correlation density

The expression of the LS coupling scheme have already been shown on the Chapter 3. We are able to express the correlation density in the jj-coupled scheme and also in the M-scheme.

The first two δ correspond to the radial part of the operator and it is trivial, in a sence that it resembles the one body density calculation, which is:

$$\rho(r) = \langle\Psi|\delta(r_1-r)|\Psi\rangle \tag{A.6}$$

In the jj coupled scheme the TBME of an operator is always given by:

$$\langle(j_0j_1)^J|O|(j_2j_3)^J\rangle = N_1N_2\left(\langle(j_0j_1)^J|O|(j_2j_3)^J\rangle - (-1)^{j_0+j_1-J}\langle(j_1j_0)^J|O|(j_2j_3)^J\rangle\right) \tag{A.7}$$

where N_1 and N_2 are normalization constants, defined as:

$$N_1 = \frac{1}{\sqrt{(1+\delta_{ab})}}$$

For the third δ in (A.5) which involves the angles, we take advantage of an identity of the δ function:

$$\delta(\theta - \theta_{12}) = sin(\theta) \sum_l \left(\frac{2l+1}{2} \right) P_l(cos(\theta)) P_l(cos(\theta_{12})) \tag{A.8}$$

We then have that:

$$\langle (j_0 j_1)^J | \delta(\theta - \theta_{12}) | (j_2 j_3)^J \rangle = \sum_l A(l,\theta) \langle (j_0 j_1)^J | \left(\frac{2l+1}{2} \right) P_l(cos(\theta_{12})) | (j_2 j_3)^J \rangle \tag{A.9}$$

where

$$A(l,\theta) = sin(\theta_{12}) P_l(cos(\theta)) \tag{A.10}$$

This is equal to:

$$\langle (j_0 j_1)^J | \delta(\theta - \theta_{12}) | j_2 j_3)^J \rangle = \sum_l A(l,\theta_{12}) \langle (j_0 j_1)^J | \left(\frac{2l+1}{2} \right) Y_l(1) Y_l(2) | (j_2 j_3)^J \rangle \tag{A.11}$$

where in the last the addition theorem of spherical harmonics was used which relates the Legendre polynomial with the spherical harmonics of particles 1 and 2. The matrix elements of the spherical harmonics are given by:

$$\begin{aligned} \langle (j_0 j_1)^J | Y_l(1) Y_l(2) | (j_2 j_3)^J \rangle \;\; = \;\; & \hat{j_0} \hat{j_1} \hat{j_2} \hat{j_3} (-1)^{j_0 + j_2 + J} \times \\ & \begin{pmatrix} j_0 & l & j_2 \\ 0.5 & 0.0 & -0.5 \end{pmatrix} \begin{pmatrix} j_1 & l & j_3 \\ 0.5 & 0 & -0.5 \end{pmatrix} \times \\ & \begin{Bmatrix} j_2 & j3 & J \\ j_1 & j_0 & l \end{Bmatrix} \end{aligned} \tag{A.12}$$

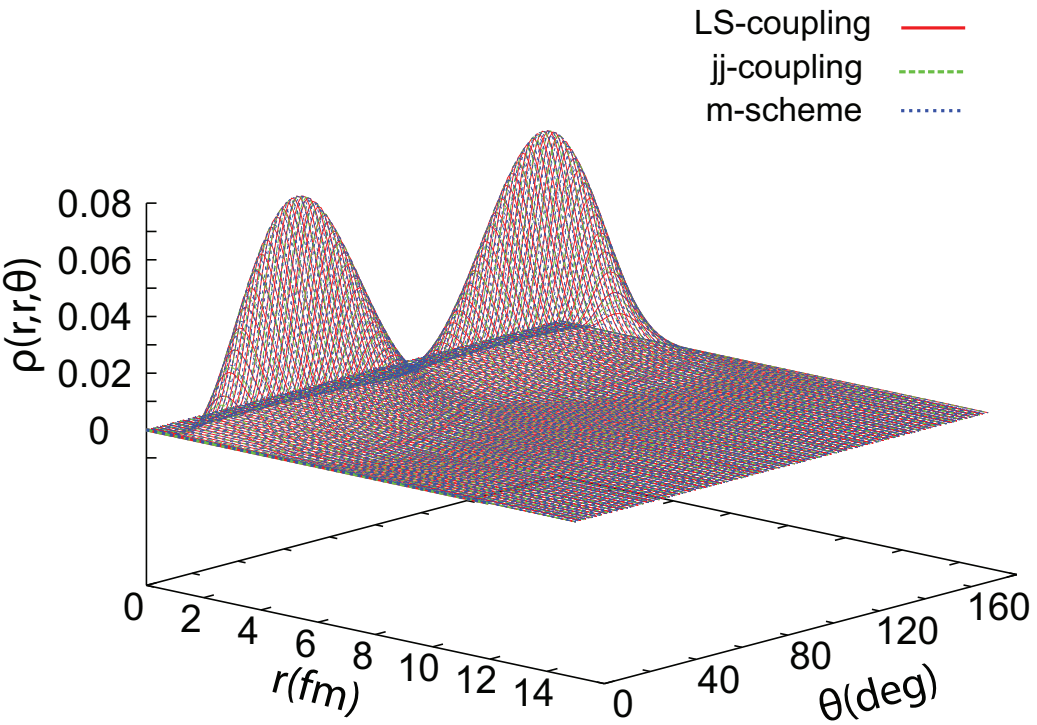


Figure A.1: Comparison of the correlation densities in three different coupling schemes.

Putting everything together and include also the antisymmetrization, the correlation density matrix elements are given by:

$$\begin{aligned}\langle (j_0 j_1)^J | \delta(r_1 - r)\delta(r_2 - r')\delta(\theta_{12} - \theta) | (j_2 j_3)^J \rangle \;=\; & \phi_{n_0 l_0 j_0}(r)\phi_{n_2 l_2 j_2}(r)\phi_{n_1 l_1 j_1}(r')\phi_{n_3 l_3 j_3}(r') \times \\ & \sum_l A(l,\theta_{12}) \langle (j_0 j_1)^J | Y_l(1) Y_l(2) | (j_2 j_3)^J \rangle \\ - & \\ & \phi_{n_1 l_1 j_1}(r)\phi_{n_2 l_2 j_2}(r)\phi_{n_0 l_0 j_0}(r')\phi_{n_3 l_3 j_3}(r') \times \\ & \sum_l A(l,\theta_{12}) \langle (j_1 j_0)^J | Y_l(1) Y_l(2) | j_2 j_3)^J \rangle \\ \times & \\ & (-1)^{j_0 + j_1 - J} \end{aligned} \tag{A.13}$$

where ϕ_{nlj} is the numerical Berggren single particle basis of the GSM. In the end we put $r = r'$ and we plot as a function of r and θ.

Notice the order of the indices in the radial wavefunctions: n_0,n_2 and n_1,n_3 for the first term and n_1,n_2 and n_0,n_3 for the second. The $\langle j_0 j_1|$ was interchanged in the second term, giving rise to the phase. Here n_0,n_1 are defining the bra and n_2,n_3 are defining the ket. Same definitions for j_0,j_1,j_2,j_3 and l_0,l_1,l_2,l_3.

The GSM code when dealing for more than two particles is constructed in the M-scheme. To express a ME of a coupled operator in the M-scheme we used the Wigner Echart theorem to express a ME in an uncoupled representation. This is the procedure we followed in order to calculate the correlation density of ^{8}He.

$$\langle j_a j_b JM|O|j_b j_d JM\rangle = \sum_{m_a m_b m_c m_d} \langle j_a m_a j_b m_b|JM\rangle\langle j_c m_c j_d m_d|JM\rangle\langle j_a j_b J||O||j_c j_d J\rangle \tag{A.14}$$

Appendix B

Benchmark calculations between GSM and Complex Scaling

		$\theta = 0$		$\theta = 0.1$	
N	size	energy (MeV)	$\langle r^2 \rangle$ (fm^2)	energy (MeV)	$\langle r^2 \exp(2i\theta) \rangle$ (fm^2)
8	180	-0.235	19.004	-0.235 -i0.002	19.022+i0.442
10	264	-0.241	19.385	-0.241+i0.002	19.398+i0.199
12	364	-0.245	19.608	-0.247+i0.001	19.616+i0.079
14	480	-0.247	19.712	-0.247+i0.0006	19.726+i0.037
16	612	-0.247	19.749	-0.248+i0.0005	19.759+i0.027
GSM		-0.249	19.820		

	GSM	Slater $\theta = 0$	Slater $\theta = 0.1$
$\langle T \rangle$	24.729	24.734	27.732-i0.007
$\langle V_{1,2} \rangle$	-2.711	-2.711	-2.710+i0.002
$\langle V_{1,3} + V_{2,3} \rangle$	-21.642	-21.647	-21.646+i0.005
$\langle$recoil$\rangle$	-0.625	-0.624	-0.623+i0.0003

Figure B.1: Energies and root mean square radii between GSM and Complex Scaling (CS).

We are presenting some benchmark calcultions between the GSM and Complex Scaling Method (CS). The two body interaction used was the Minnesota interaction in its original form (no fitting was made) and the one-body potential was the KKNN [125] which has the following form:

$$V(r) = \sum_{i=1}^{2} V_i^c \exp(-\mu_i^c r^2) + (-1)^l \sum_{i=1}^{3} V_{li}^c \exp(-\mu_{li}^c r^2) + \boldsymbol{\sigma}\cdot\boldsymbol{l}\left(V^{\sigma l}\exp(-\mu^{\sigma l} r^2) + (1+0.3(-1)^{l-1})\sum_{i=1}^{2} V_i^{\sigma l}\exp(-\mu_{li}^{\sigma} r^2)\right) \tag{B.1}$$

The parameters where determined by fit on available neutron/proton α elastic scattering phase shifts. In the particular calculation the CS ^{6}He wavefunction was assumed to be given as a superposition of Slater orbits:

$$\Psi(^6He) = \sum_{l_1 j_1}\sum_{l_2 j_2}\sum_{ij=0}^{N} C_{l_1 j_1 l_2 j_2}\mathcal{A}\left(r_1^{l_1+i} r_2^{l_2+j}\exp(-\alpha(r_1+r_2))[\mathcal{Y}_{l_1 j_1}(\hat{\boldsymbol{r}}_1)\mathcal{Y}_{l_2 j_2}(\hat{\boldsymbol{r}}_2)]^{JM}\right) \tag{B.2}$$

where N is the radial quantum number of the Slater basis and the expansion coefficients are determined by the diagonalization of the Hamiltonian. The exponential nature of the Slater basis reassures the correct asymptotic behavior of the system. The basis idea behind the CS is the transformation the radial coordinates (COSM system) according to $\boldsymbol{r}_i \rightarrow \boldsymbol{r}_i \exp(i\theta)$, where θ is the scaling angle. Then the Hamiltonian is transformed into the complex scaled one H^θ and one needs to solve a complex scaled eigenvalue problem:

$$H^\theta \Psi^\theta = E^\theta \Psi^\theta \tag{B.3}$$

The solutions of these eigenvalue problem are many-body resonant and non-resonant states. This approach is similar to the GSM but the main difference is that in GSM the Hamiltonian is Hermitian and the Hamiltonian matrix becomes after it is diagonalized in a complex s.p basis. In CS on the other hand the Hamiltonian is non-Hermitian (complex scaled Hamiltonian), but the s.p basis is real.

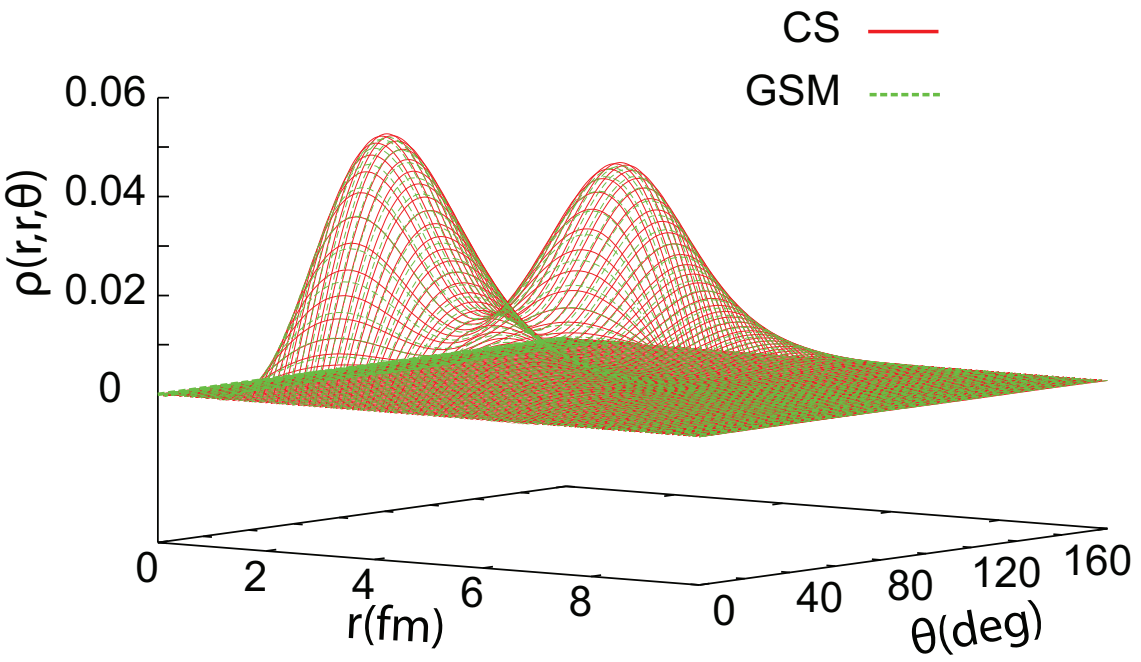


Figure B.2: Comparison of correlation densities between GSM and Complex Scaling (CS).

In Fig.B.1 we present energies and root mean square radii which were calculated in the GSM and CS. The model space was consisting of five partial waves in the p-sd configurational space. In the bottom we calculated the decomposition of the Hamiltonian and the results are identical up to the second/third digit. In Fig.B.2 we plot the correlation densities.

Vita

George Papadimitriou was born in Greece, a Sunday morning on June 27, 1982. Even though he had an obvious talent in basketball where he reached a semi-professional level in the age of sixteen, he decided that Physics is the career that he wants to follow. In 2000 he entered the Physics Department of the Aristotle University of Thessaloniki, Greece where he graduated in 2005 with a GPA of 8.71/10. Soon after that, in 2006, he joined the Department of Physics and Astronomy at the University of Tennessee, Knoxville, under the supervision of Professor Witek Nazarewicz. During his stay at UT he was the author of two articles and one conference proceeding paper and also co-author of a third article. He also had the chance to present numerous talks in international conferences and workshops. He expects his Ph.D. on December 2011.